

# WIRELESS INTERROGATION OF PASSIVE CRACK SENSOR

By

Xu Zhen

A thesis submitted in partial fulfillment of the requirements for the degree of

MASTER OF SCIENCE

In

MECHANICAL ENGINEERING  
UNIVERSITY OF PUERTO RICO  
MAYAGÜEZ CAMPUS  
December, 2010

Approved by:

---

Ricky Valentin, Ph.D.

Member, Graduate Committee

---

Date

---

Genock Portela, Ph.D.

Member, Graduate Committee

---

Date

---

Yi Jia, Ph.D.

President, Graduate Committee

---

Date

---

Ana Gonzalez, Ph.D.

Representative of Graduate Studies

---

Date

---

Gustavo Gutierrez, Ph.D.

Chairperson of the Department

---

Date

## **ABSTRACT**

As crack location and length is one of the key performance parameters that affects the life of mechanical components and civil structures, crack sensing has become one of the most vital technologies in structure health monitoring. It is desirable that the sensor can be non-obtrusively embedded into the structures or systems to be monitored, whereas, no physical connections for power supply or data acquisition is required.

The primary objective of the project is to conduct basic research into the crack sensing mechanism of the proposed passive wireless sensor, aiming at developing a novel crack micro-sensor and fabrication of associated electronics for remote power supply and wireless data acquisition.

To this end, a passive wireless crack sensor, being able to operate in crack detecting, has been developed in this research project. The design of the sensor comprises of two major components: an interdigital capacitor (IDC) serving as cracking sensing element and a spiral inductor functioning as passive power source and communication unit. The sensor is activated by electromagnetic wave. The frequency response of the sensor can be monitored by interrogating the sensor remotely with a single loop antenna. The employment of inductor eliminates the conventional wire connection for power supply and data transmission. A model has been established to simulate the sensor working mechanism. With this model, the relationship between resonant frequency of the sensor and crack formation and developing effect was thoroughly investigated.

Moreover, sensor performance was analyzed to optimize the sensor configuration, maximize sensing distance, Q factor and sensitivity. The sensor prototype was then successfully fabricated to demonstrate the concept of a crack sensing device using passive wireless communication.

## RESUMEN

La instrumentación para identificar y medir grietas a pasado a ser una de las tecnologías vitales para monitorear la condición existente de estructuras. Es deseable que los sensores de estas tecnologías puedan ser adheridos a estructuras sin que se requiera ningún tipo de conexión física, proveedores de energía, ni sistemas de adquisición de datos.

El objetivo principal de este proyecto es llevar a cabo investigación fundamental dentro del área de identificación de grietas, específicamente un sensor inalámbrico pasivo. Este objetivo está orientado al desarrollo de un microsensor, incluyendo la fabricación de sus componentes electrónicos, los cuales tendrán capacidad de recibir energía remota y adquirir datos en forma inalámbrica.

En el presente proyecto se desarrolló un detector de grietas inalámbrico que consiste en 2 componentes principales: un capacitor interdigital (IDC) que trabaje como elemento sensorial de agrietamiento y un inductor espiral que sirve como fuente de energía pasiva y unidad de comunicación. El sensor se activa por ondas electromagnéticas y su respuesta en frecuencia es monitoreada por la acción remota de una antena de circuito simple.

El desempeño del sensor fue analizado con el fin de optimizar su configuración, maximizar la distancia sensorial, estudiar el factor Q y su sensibilidad. Un prototipo fue construido para demostrar el dispositivo de detección de grietas usando comunicación inalámbrica pasiva.

## ACKNOWLEDGEMENTS

I wish to express my deep gratitude to my thesis advisor, Professor Yi Jia, for his invaluable advice and steadfast support throughout this thesis project. I feel extremely lucky to have a chance to study novel sensor development under his guidance. I am also grateful for his encouragement that helped me overcome all sorts of technical and personal obstacles during my research work.

I also like to thank Dr. Genock Portela for his generous help in providing the laboratory equipment required for my thesis. In addition, I would like to thank Dr. Ricky Valentin for his highly supportive encouragements as a member of my graduate committee.

At last, but the most importantly, I would like to thank my family, for their unconditional support, inspiration and love.

Funding and resources for the development of this research were provided by NSF Grant 0549338 and DE-FG26-07NT43061.

# TABLE OF CONTENTS

<b>ABSTRACT</b> .....	<b>II</b>
<b>RESUMEN</b> .....	<b>III</b>
<b>ACKNOWLEDGEMENTS</b> .....	<b>IV</b>
<b>LIST OF TABLES</b> .....	<b>VII</b>
<b>LIST OF FIGURES</b> .....	<b>VIII</b>
<b>LIST OF SYMBOLS</b> .....	<b>XI</b>
<b>1 INTRODUCTION</b> .....	<b>1</b>
1.1 Background .....	1
1.2 Proposed Passive Wireless Crack Sensor .....	2
1.3 Advantages of the Passive Wireless Sensor .....	3
1.4 Research Objectives .....	4
1.5 Thesis Organization .....	4
<b>2 LITERATURE REVIEW</b> .....	<b>5</b>
2.1 Fatigue crack mechanism .....	5
2.2 Current technology for crack sensing .....	7
2.2.1 EPD crack sensor for structural surface .....	7
2.2.2 Fiber optic crack sensor .....	8
2.2.3 Mobile fiber ultrasonic sensor .....	9
2.2.4 Magnetic particle testing .....	10
2.2.5 Infrared and thermal testing .....	11
2.2.6 Crack propagation sensor .....	11
2.2.7 Strain gauge sensor for crack monitoring .....	12
2.2.8 ECT testing sensor for crack detection .....	13
2.3 Conclusions .....	15
<b>3 CRACK SENSING ELEMENT DESIGN</b> .....	<b>16</b>
3.1 Parallel Plate Capacitor .....	16
3.2 Interdigital Capacitor .....	18
3.2.1 IDC analysis model .....	18
3.3 Geometry Dependent Capacitance .....	23
3.4 Crack Dependent Capacitance .....	27
3.4.1 Crack parameters in IDC sensor .....	27
3.4.2 Crack angle definition .....	27

3.4.3 Crack length definition.....	28
3.4.4 Discussion.....	30
3.5 Conclusions .....	39
<b>4 SENSOR ANTENNA DESIGN.....</b>	<b>40</b>
4.1 Spiral Inductor .....	40
4.2 Coupling Factor .....	42
4.3 Q-factor .....	43
4.4 Conclusions .....	45
<b>5 RRMOTE POWER AND WIRELESS COMMUNICATION .....</b>	<b>46</b>
5.1 Inductive Powering .....	46
5.2 Modeling and Simulation.....	48
5.3 Resonant Frequency.....	52
5.4 Conclusions .....	53
<b>6 SENSOR CHARACTERIZATION AND EXPERIMENT RESULTS .....</b>	<b>54</b>
6.1 Fabrication interdigital crack sensor.....	54
6.2 Testing System Setup.....	57
6.2.1 Pretest procedure .....	57
6.2.2 Actual crack test setup.....	58
6.3 Sensor Performances Characterization .....	60
6.3.1 Theoretical calculation.....	60
6.3.2 Experiment result .....	61
6.3.3 Measurements vs. theoretical result.....	63
6.4 Conclusions .....	64
<b>7 CONCLUSIONS AND FUTURE WORK.....</b>	<b>65</b>
7.1 Conclusions .....	65
7.2 Future work .....	65
<b>REFERENCE .....</b>	<b>67</b>

## LIST OF TABLES

<b>Table</b>	<b>Page</b>
3-1 Detailed equations needed for the calculation of $C_E$ and $C_I$ .....	-22-
3-2 Electrical Parameter Values.....	-29-
5-1 Electrical Parameter Values for IDC crack sensor.....	-51-
6-1 Frequency data set for the experiment.....	-59-

## LIST OF FIGURES

<b>Figure</b>	<b>Page</b>
1-1 Proposed wireless passive crack sensing system.....	-2-
1-2 Proposed Wireless Sensor Scheme.....	-3-
2-1 Wood's model for fatigue crack initiation.....	-6-
2-2 System scheme of electric potential detection for structural crack.....	-8-
2-3 Concept of distributed sensing with the novel sensor.....	-9-
2-4 FGB sensor measuring system.....	-9-
2-5 (a) Crack propagation pattern (b) Measure resistance between A and B.....	-11-
2-6 Diagram of strain gauge sensor for micro-crack monitoring system.....	-12-
2-7 Outline of eddy current test.....	-14-
3-1 A parallel-plate capacitor.....	-16-
3-2 The electric field between the plates of a parallel-plate capacitor.....	-17-
3-3 Operating principle of interdigital sensor.....	-18-
3-4 Layout of electrode plane.....	-19-
3-5 Cross-section of IDC geometric dimensions.....	-19-
3-6 Half unit cell model of the proposed multilayer interdigital capacitor.....	-19-
3-7 The equivalent circuit of the top air interdigital capacitor.....	-21-
3-8 Splitting of the proposed three layered IDC.....	-21-
3-9 Capacitances as a function of $\eta$ and $r$ .....	-25-
3-10 Capacitances as a function of $L_C$ and $N_C$ .....	-26-
3-11 Parameter of IDC sensor.....	-27-
3-12 Crack orientation.....	-28-
3-13 Unit crack length simulation.....	-29-
3-14 Arbitrary crack Initial location $x_1$ .....	-30-
3-15 IDC capacitances vs. Arbitrary crack Initial position $x_1$ .....	-30-
3-16 Different crack initial position $x_1$ and arbitrary crack propagation angle .....	-31-
3-17 IDC capacitances vs. different crack initial position $x_1$ and arbitrary crack	

propagation angle $\theta$ .....	-32-
3-18 Arbitrary crack initial position $x_1$ and propagate at certain angle $\theta$ .....	-33-
3-19 IDC capacitances vs. arbitrary crack initial position $x_1$ and certain crack propagation angle $\theta$ .....	-33-
3-20 IDC capacitances vs. different crack initial position $x_1$ and arbitrary crack propagation angle $\theta$ (N=4).....	-34-
3-21 Different crack initial position $x_1$ and arbitrary crack propagation angle $\theta$ .....	-35-
3-22 (a) IDC capacitances vs. different crack initial position $x_1$ and the crack propagate at angle of $45^\circ$ for different crack size N.....	-36-
3-22 (b) IDC capacitances vs. different crack initial position $x_1$ and the crack propagate at angle of $90^\circ$ for different crack size N.....	-36-
3-22 (c) IDC capacitances vs. different crack initial position $x_1$ and the crack propagate at angle of $135^\circ$ for different crack size N.....	-36-
3-23 (a) IDC capacitances vs. different crack initial position $x_1$ and the different crack propagation angle for crack size N=2.....	-37-
3-23 (b) IDC capacitances vs. different crack initial position $x_1$ and the different crack propagation angle for crack size N=3.....	-37-
3-23 (c) IDC capacitances vs. different crack initial position $x_1$ and the different crack propagation angle for crack size N=4.....	-38-
4-1 Schematic View of Spiral Inductor.....	-40-
4-2 Inductance vs. Coil Mean Radius.....	-41-
4-3 Coupling coefficient $k$ vs. $d$ and $R_s$ .....	-42-
4-4 Radius of sensor inductor design result.....	-43-
4-5 Q-factor vs. Resistance & Inductance.....	-44-
5-1 Inductively Coupled Circuit.....	-47-
5-2 Inductive coupled reader and LC sensor.....	-49-
5-3 Equivalent circuit diagram of wireless telemetry system.....	-49-
5-4 Magnitude & Resonant frequency.....	-51-

5-5 Resonant frequency of Input impedance vs. Crack propagation.....	-52-
6-1 Splitting of the proposed IDC sensor.....	-56-
6-2 Fabricated sensing element prototype.....	-56-
6-3 Crack sensor bonded to the testing coupon.....	-57-
6-4 Propose test coupon mounted in test apparatus.....	-58-
6-5 Sensor coil vs. reader antenna.....	-58-
6-6 Experiment setup.....	-59-
6-7 Actual crack path (N=8).....	-60-
6-8 Resonant frequency of theoretic result.....	-61-
6-9 Resonant frequency of IDC sensor with crack propagation.....	-62-
6-10 Resonant frequency of experimental result.....	-62-
6-11 Comparison between experiment result and theoretic result.....	-63-

## LIST OF SYMBOLS

SYMBOL	NAME	UNIT
$A$	Sensing area of the sensor	$mm^2$
$a$	Coil wire radius	$mm$
$C_R$	Capacitance of the reader	$F$
$C_S$	Capacitance of the sensor	$F$
$f$	Resonant frequency	$Hz$
$I_1$	Current on the reader antenna	$A$
$I_2$	Current on the sensor	$A$
$k$	Coupling Coefficient	/
$L_R$	Inductance of the reader	$H$
$L_S$	Inductance of the sensor	$H$
$M$	Mutual inductance	$H$
$N$	Turns of coils	/
$R$	Coil hoop radius	$mm$
$R_R$	Self resistance of the reader	$\Omega$
$R_S$	Self resistance of the sensor	$\Omega$
$t$	Thickness of the sensing material	$mm$
$\epsilon_0$	Permittivity of free space $8.85 \times 10^{-12}$	$F/m$
$\mu_0$	Magnetic permeability of free space $4\pi \times 10^{-7}$	$H/m$

# 1 INTRODUCTION

In this chapter, a brief background introduction of this thesis project will be presented. Thereafter, we state the objective of our research project, which is the demonstration of a novel passive wireless crack sensor. Finally, the structure of the thesis is outlined.

## 1.1 Background

In the recent years there has been an increasing interest in the use of sensing technologies for Structural health monitoring (SHM). SHM is the process of detecting and monitoring structural damages [1-4]. All structures undergo a process of damage and deterioration over a period of time. Due to extreme changes occurs in its operational environment, deterioration will be accelerated and ultimately lead to collapse of the whole structure. The resulted loss of human life and property can be devastating. Thus, it is of utmost importance to monitor the structural health of civil, aerospace structures to improve their reliability. SHM is especially important for those structures that are operating beyond their designed service life. SHM involves observation of the structure using one or more distributed sensors monitoring one or more properties of the structure. Some of the important properties that are used to quantify the health of a structure are fatigue cracks, strain, temperature and displacement. Among them, fatigue crack is considered as the major defects that emerge due to aging of structures.

In mechanics of materials, fatigue is the progressive and localized structural damage that occurs when a material is subjected to cyclic loading. If the loads are above a certain threshold, microscopic cracks will begin to form at the surface. Eventually a crack will reach a critical size, and the structure will suddenly fracture. A significant reduction in mechanical performance of the materials will cause destructive security problems.

Currently, various crack detection techniques are being researched, developed, and evaluated for detecting fatigue damage, including ultrasonic testing [5], infrared and thermal imaging [6], acoustic emission [7], eddy current methods [8], magnetic particle testing, radiographic testing, fiber optic sensors [9], piezoelectric sensors [10] and various crack propagation gages. However, most of these techniques are not commercially feasible because of the complex fabrication and interrogation processes and the high costs involved. There is a demand for wireless sensors for SHM that can be fabricated using low-cost processes. This thesis describes a simple and cost-effective design of passive, wireless crack sensing elements that can be applied for the detection of cracks in SHM.

## 1.2 Proposed Passive Wireless Crack Sensor

In this thesis, a novel passive wireless sensor, consisting of an interdigital sensing capacitor and a loop antenna as inductor antenna is proposed for crack monitoring. The abovementioned two components work together as an LC resonator whose resonant frequency is designed to change correspondingly with the size, shape, orientation, propagation and stages of the monitored crack. This corresponding frequency variation will be detected by a LC frequency reader by monitoring the impedance across the terminals of the wide bandwidth reader antenna. Thereafter, this crack information will be retrieved and interpreted based on the received signal from this reader by the resonant frequency shift.

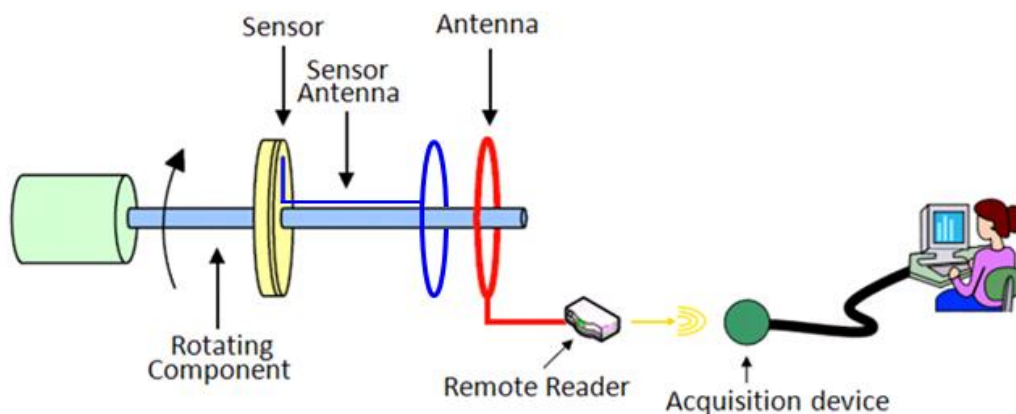


**Figure 1-1 Proposed wireless passive crack sensing system**

In this project, crack monitoring will be accomplished by teaming up interdigital crack sensor and the remote reader. The crack signal is conveyed by the forms of the resonant frequency acquired by a remote antenna. Here, the remote antenna has dual function. While it performs the wireless communication, it also serves as a remote power supply for the sensor.

The power delivery and wireless data communication scheme is illustrated in Figure 1-2. As common practice shown in the figure, an oscillating magnetic wave will be sent out through the remote reader, and will be received by sensor inductor coil by inductive link, thus active on the LC sensor. In the meantime, the frequency modification of LC sensor induced by crack formation and propagation can be detected by the remote reader.

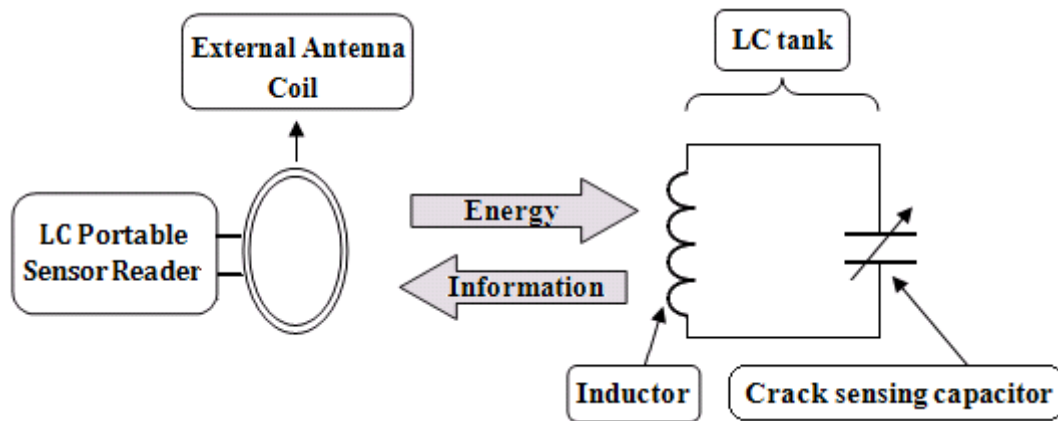


Figure 1-2 Proposed Wireless Sensor Scheme

### 1.3 Advantages of the Passive Wireless Sensor

The major advantage of this proposed crack sensing technology lies in that the sensor technology can be non-obtrusively embedded into the structures or systems to be monitored, whereas, no physical connections for power supply or data acquisition is required. Its main features can be outlined as follows:

- (1) No need of physical contacts and associated electronics on the sensor board;
- (2) Establishing a capacitive frequency-encoded sensing mechanism based on LC circuit;
- (3) Integrating a wireless sensor and inductive powering into multilayered structure;

## **1.4 Research Objectives**

The primary objective of the proposed project is to conduct basic research into the crack sensing mechanism of the proposed passive wireless sensor, aiming at developing a novel crack sensor and fabrication of associated electronics for remote power supply and wireless data acquisition. In particular, the proposed project is set out to accomplish the following objectives:

- (1) Develop an innovative powered telemetry sensor scheme;
- (2) Design and fabricate prototypes of proposed sensor;
- (3) Design a wireless capacitive crack sensor and simulate its small sized counterpart.
- (4) Characterize and calibrate the sensor performance;

## **1.5 Thesis Organization**

The thesis consists of seven Chapters. In Chapter 2, the existing crack sensing technologies will be widely reviewed, and modern techniques involved in crack sensing will be compared with sensing principles and various applications. Chapter 3 presents physical model of the interdigital capacitor as the crack sensing element and analyzing all the contribution of geometry properties to the change of the capacitance. Chapter 4 concentrates on Spiral inductor study. In order to enhance the sensor performance, the design of the antenna will be simulated respect to the quality factor and coupling factor. Chapter 5 demonstrates the remote power and wireless communication and the working performance together with the interdigital capacitor. Chapter 6 covers sensor fabrication, experimental setup and a sensor characterization with respect to resonant frequency, quality factor, coupling factor and many others. Finally, Chapter 7 summarizes the contributions of the work and the future improvements of the crack sensor technology.

## **2 LITERATURE REVIEW**

As crack location and length is one of the key performance parameters that affects the life of mechanical components and civil structures, crack sensing has become one of the most vital technology in areas such as SHM, damage detection, condition-based maintenance, failure prevention and non-destructive evaluation. In this chapter, the first section discusses the mechanism of the fatigue crack it is understood by today, and then several newly developed technologies of crack sensing in the last several years will be reviewed. Advantages of our proposed sensor will be highlighted.

### **2.1 Fatigue crack mechanism**

Fatigue is a localized damage process of a component produced by cyclic loading and is a cumulative process which includes crack nucleation, short crack growth, long crack growth and final fracture. The nature of a fatigue crack is that localized plastic deformations usually occur at the crack tip (the highest stress site), while elastic deformations occur at other regions. Component will fail as a result of increasing length of the crack [11]. Fatigue cracks can initiate on localized shear planes at or near high stress concentrations, inclusions, porosity or discontinuities. There are several equivalent models available to explain the initiation of fatigue cracks [12]. Wood's model, which is shows that during loading, slip occurs on a favorably oriented plane, and during unloading slip takes the reverse direction on a parallel slip plane. The slip on the first plane is restrained by strain hardening and oxidation due to the newly created free surface resulting in an extrusion or an intrusion in the metal surface. An intrusion created in this way can grow into a crack by continuous loading cycles.

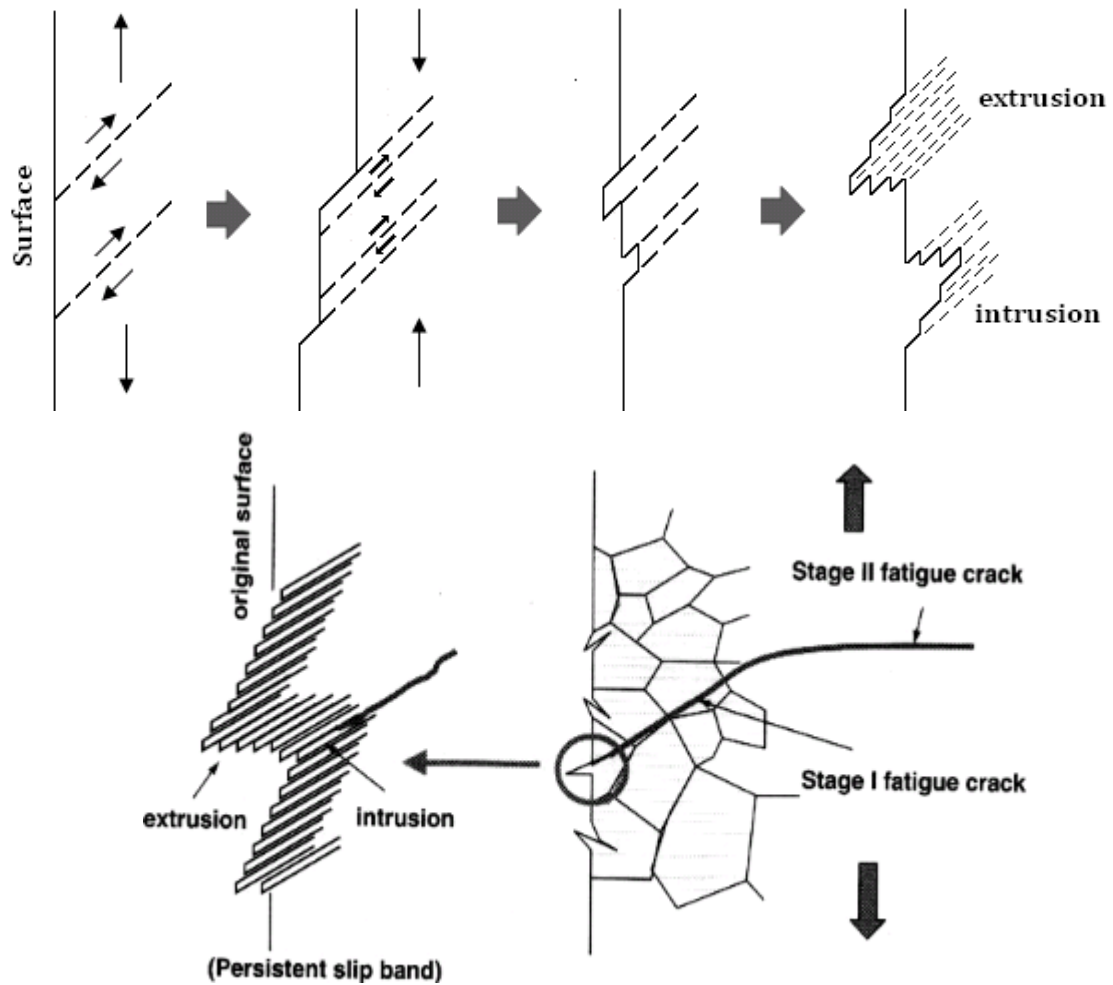


**Figure 2-1 Wood's model for fatigue crack initiation**

Once the crack nucleation starts, and the cyclic loading continues, the crack tends to grow along the plane of maximum shear stress and through the grain boundary. The crack growth is divided into two stages. Stage I is the initial, short finite length crack growth and its crack tip plasticity is mostly affected by the grain size, type of slippage, orientation and the stress level. Stage II crack growth refers to long crack propagation normal to the principal tensile stress plane (See Figure 2.2). The crack tip plastic zone in Stage II crack is much larger than the material microstructure thus they are less affected by the properties of the material microstructure. In general, for engineering components, crack initiation period refers to the total nucleation and propagation of the short cracks, whereas crack propagation period refers to the growth of the long cracks.

## 2.2 Current technology for crack sensing

Different types of crack sensing technologies are being developed to detect fatigue crack for SHM system. These methods are based on different approaches and utilize diverse technologies for fatigue detection. Here, several newly developed technologies of crack sensing in the last several years will be reviewed.

### 2.2.1 EPD crack sensor for structural surface

Recently, electric potential detection (EPD) method is an available approach to make detection of the micro-damage crack on structural surface possible. First, EPD is feasible for detection of structural surface crack because it can be expediently actualized in covert or in capacious place of structures. Second, its theory and technical plants are simple. People have early paid attention to monitor crack damage on structural surface via EPD method in 1992 [13].

The principle of EPD method is based on the conductivity of metal materials [14]. When the current passes through the test part of a structure, there will be a detectable potential field produced in this part. Ohm's law  $U= IR$  governs the electric potential difference between some two points on this test part. If the current value  $I$  is constant, the potential difference value  $U$  only depends on the resistance value  $R$ . If the shape and size of the structure, the property of the material, and so on, is kept invariable, the value  $R$  will change with the crack occurrence in the test part of structure. Therefore, one can correlated the crack occurrence and its status with the electric potential difference values varied with the change of crack shape or size. Generally, the system for EPD consists of electric source, probes, circuit and display, etc. The alternating electric field in the detected part is established through electrifying the part by input probes, and the measured signals of the electric potential are picked up by output probes. A typical system scheme for EPD is shown in Figure 2-1. The four probes are placed along a beeline on the detected part of structure. The A and B are input probes and c and d are measuring output probes. Suppose that the electric potential difference values are  $U_0$

and  $U_R$  between c and d point, respectively, without a crack and with a crack, and the input current values for two cases are the same, the existing crack will bring to an electric potential difference. One can estimate the crack based on this signal of measured electric potential difference.

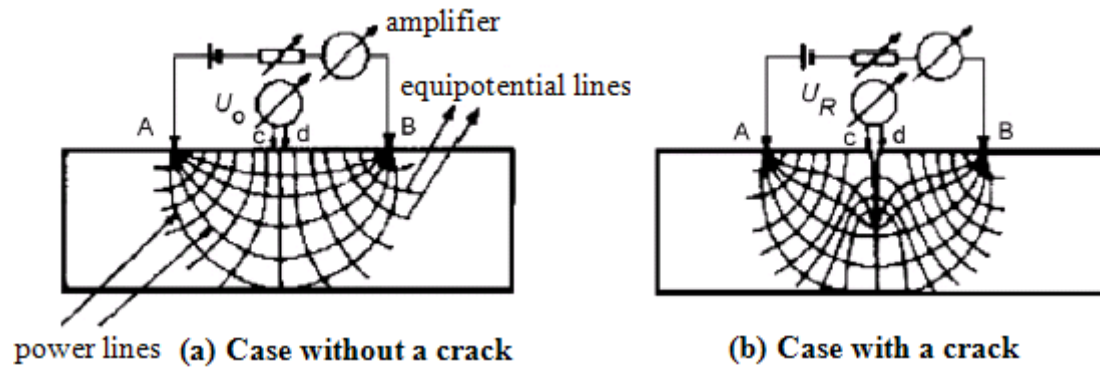


Figure 2-2 System scheme of electric potential detection for structural crack [14]

### 2.2.2 Fiber optic crack sensor

The use of fiber-optic sensors in SHM is gaining popularity for many reasons. Their light weight, flexibility in size, and resistance to electromagnetic fields has made them popular over other conventional sensors [15]. They can be bonded to steel structures or embedded in composites for real time monitoring in in-service structures

The principle of the sensor is illustrated in Figure 2-4. An optical fiber can hence be coupled to the structure in such a way that it is inclined to the crack (Figure 2-4). Once the crack opens, the optical fiber needs to bend to maintain its continuity as shown in the inset of Figure (a). The bend will induce loss of light power from the fiber core to the surroundings. As a result, the transmitted light in the fiber core, as well as the backscattered optical signal, will both exhibit a sudden drop across the crack. By utilizing the optical time domain reflect meter (OTDR), which measures the Rayleigh backscattered signal as a function of time, we can locate the crack positions from the time corresponding to the signal loss (distance = time  $\times$  light velocity in the waveguide) and the crack opening from the magnitude of the drop. A typical plot of the backscattered signal versus time, both before and after crack formation, is shown in

Figure (b). Before any crack forms, the gradual decline of the backscattered signal is solely due to attenuation. At the turning points of the fiber, power loss may also be observed. To minimize these losses, the curvature at the turning points should be reduced. After the cracks open, sharp drops correspond to the crack locations along the fiber will appear in the plot.

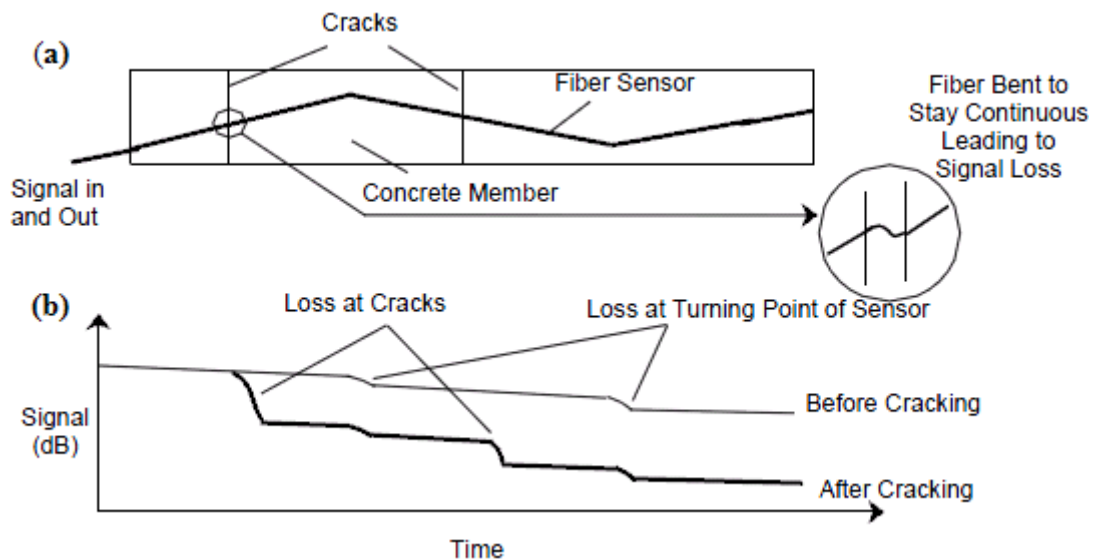


**Figure 2-3 Concept of distributed sensing with the novel sensor [16]**

### 2.2.3 Mobile fiber ultrasonic sensor

Ultrasonic inspection technique has been commonly applied to crack detection as described in Refs [17-18]. Ultrasound traveling across fatigue crack is scattered at the crack surface. As a result, the response signal shows a different behavior from the reference signal detected in intact area. Ultrasonic testing is commonly used in aerospace and automotive industries and consists of four different types of waves: longitudinal or compressive waves, compressive and shear waves, surface or Rayleigh-waves, and plate or Lamb-waves.

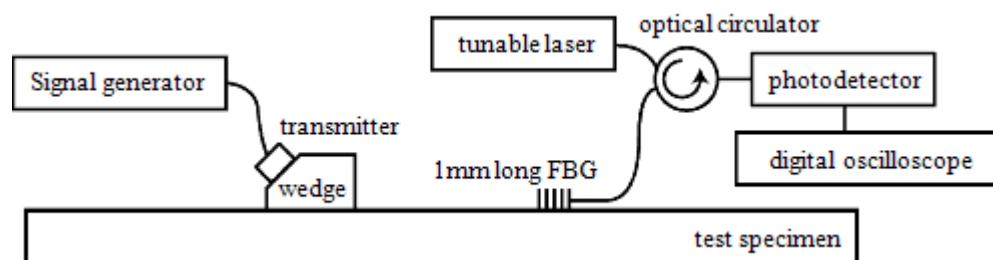


**Figure 2-4 FBG sensor measuring system [19]**

According to Refs [18], the principle of ultrasonic detection using FBG sensors with laser light source has been described. The measuring system is shown in Figure 2-3. The FBG employed had a grating length of either 1 or 12 mm and a diameter of 135 $\mu$ m with polyimide coating. Laser light at the wavelength where the reflectivity of the FBG was reduced by half was launched into the FBG sensor via an optical circulator. The light reflected from the sensor traveled to a photo-detector where intensity of light was converted into voltage signal. The photo-detector output corresponding to ultrasonic response was averaged 512 times and recorded in a digital oscilloscope at a sampling speed of 1 GHz.

In conventional ultrasonic inspection, piezoelectric devices have been used to detect ultrasound. However, the piezoelectric sensors have disadvantages that they suffer from electromagnetic interference and cannot be used in inflammable atmosphere.

#### *2.2.4 Magnetic particle testing*

Magnetic Particle Testing (MT) is another inspection method used to identify or confirm fatigue cracks, especially in welds. This method is mostly used to detect surface cracks. However, sub-surface cracks also can be detected if the depth is not too large. The MT procedure involves surface preparation, magnetization, application of particles, removal of excess, post cleaning and demagnetization [5]. Fine magnetic particles when sprayed on the component will detect distortions in the steel that occur as a result of a distorted magnetic field due to cracking. In the presence of damage, these particles form clusters at crack tip locations [20]. These magnetically held clusters of particles generally indicate its location, size, shape and extent [7]. The major limitation of this method is that non-ferromagnetic materials such as aluminum (Al) alloy, magnesium (Mg) alloy, copper (Cu) alloy, lead (Pb), titanium (Ti) alloy and austenitic stainless steels cannot be tested using MT.

### 2.2 5 Infrared and thermal testing

Infrared and Thermal Testing (IR) is used as another NDE method to detect fatigue cracks in metals. An IR scanning system can measure and view temperature patterns based upon temperature differences as small as a few 100ths of a degree Centigrade and it can be performed during day or night [6], depending on environmental conditions and the type of application. According to [21], Small Business Innovative Research (SBIR) has developed a high-resolution thermo-graphic imaging system to detect surface-breaking fatigue cracks. This forced diffusion thermograph method uses a high-wattage light to heat the desired surface. A pattern of hot and cold regions is created on that surface as a result which can be indentified via thermo-graphic imaging system and in the presence of a crack, the characteristic pattern is observed.

### 2.2.6 Crack propagation sensor

Using a crack propagation pattern to detect elongation of crack is a technique exists to detect the growth of a crack electronically [22].

The pattern made up by: a brittle, paper-thin coupon containing a ladder-like pattern of electrically conductive material. When such a sensor is bonded to a section of material near the tip of a crack, as shown in Figure 2-5, the individual rungs of the sensor will break as the crack passes through them. This will change the electrical resistance measured between the sensor's two terminals, as shown in Figure 2-4.

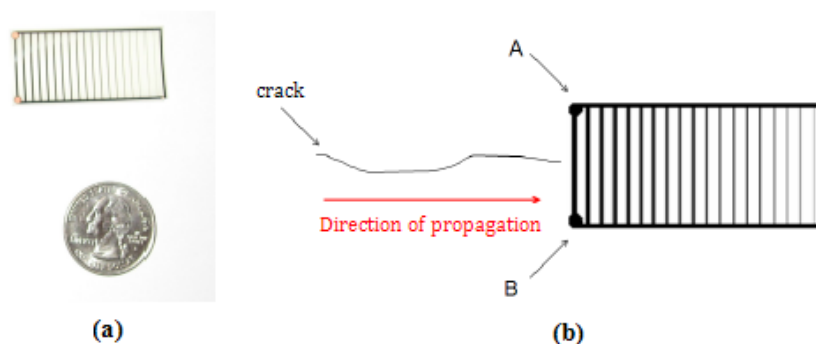


**Figure 2-5 (a) Crack propagation pattern (b) Measure resistance between A and B [22]**

A crack propagation pattern was bonded to a small test coupon composed of A36 steel. This coupon was fabricated with a wire-cut notch such that when the coupon was properly manipulated in materials testing apparatus, a crack would grow and propagate through the portion of the coupon to which the sensor was attached. The testing apparatus applied force to the coupon by applying and releasing tension through two circular attachment points at the top and bottom of the test coupon. All displacements and forces are measured with respect to these two points.

### 2.2.7 Strain gauge sensor for crack monitoring

Strain gages are still widely used as reasonable indicators of structural health and help to determine damage due to fatigue [23-25].

Cracks are monitored based on the change or variation of strain values by wireless network system which is shown in Figure 2-6 [26].

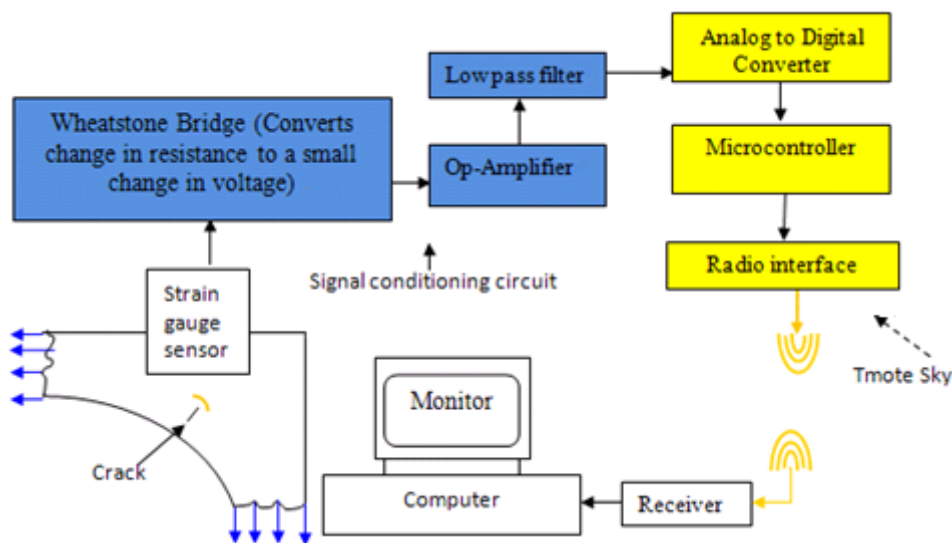


**Figure 2-6 Diagram of Smart Wireless Sensor for Micro-Crack Monitoring System [26]**

Wireless strain gages deploy the same principle of typical strain gages but use wireless transmission of the signal. In addition, battery power, on board memory storage and on board bridge completion resistors are some of the features of wireless strain gages. Crack Propagation Gages, a development of typical strain gages, provide a

convenient method for indicating the rate of crack propagation when applied to a structure.

These gages consist of a number of resistor strands that are connected in parallel [27]. Progressive fracture of the strands due to crack propagation creates open circuiting while increasing the total resistance, which can be measured by using a strip chart recorder. Crack-First is another recently developed patented fatigue sensor to detect fatigue damage in welded structures [28]. Based on fracture mechanics principle, this sensor is made of a thin steel coupon with a pre-crack at the center and is meant to be attached to a structure adjacent to the critical weld detail. When the structure undergoes cyclic loading, the crack propagates. This is especially developed for welded joints, where the presence of flaws acts as fine cracks at the weld toe and largely eliminates the crack initiation phase. FHWA has developed a device named the Passive Fatigue Load Measurement Device with a similar principle for the purpose of estimating the fatigue loads in bridges. This device has two pre-cracked Al fatigue coupons that strain along with the bridge. Due to the difference in grades of these coupons, cracks will grow at different rates. By periodically measuring the crack length using another meter for a length of time, the fatigue life of the bridge under variable amplitude loading can be determined [29].

#### *2.2.8 ECT testing sensor for crack detection*

Eddy current testing has its origins with Michael Faraday's discovery of electromagnetic induction in 1831. In 1879 Hughes recorded changes in the properties of a coil when placed in contact with metals of different conductivity and permeability, but it was not until the Second World War that these effects were put into practical use in testing materials. Much work was done in the 1950's and 60's, particularly in the aircraft and nuclear industries and Eddy Current testing is now widely used in these fields.

Although Eddy Currents are a problem in electrical engineering systems such as transformers, as they are cause of severe heating losses, they are used to advantage in this non-destructive testing.

Eddy current testing is based on the principles of electromagnetic induction. In this technique, following the Faraday's law, a coil is excited with alternating current, which induces current with circular paths (eddy current) in an electrically conductive testing material when the energized coil is placed near its surface. Damages, defects and material properties variations are detected as changes in the coil impedance that arise due to distortion or perturbations of the eddy currents at regions of discontinuities.

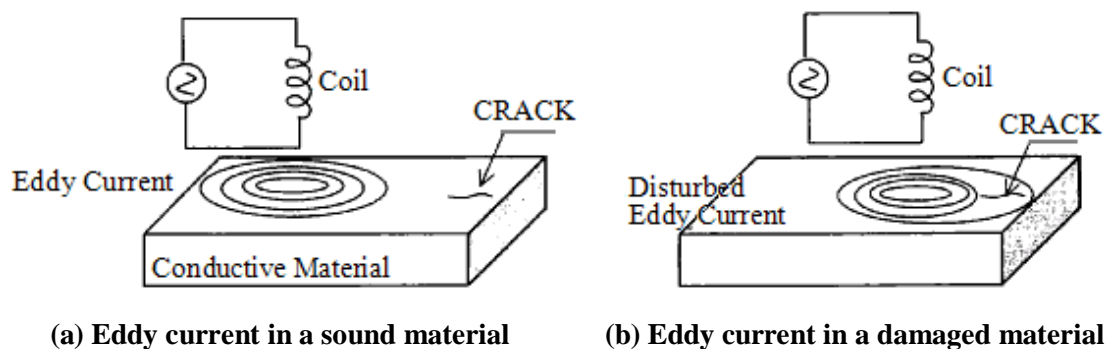


**Figure 2-7 Outline of Eddy current test [30]**

As shown in Figure 2-11, the currents induced in a metal surface oscillate in a circular pattern, flowing in a direction opposite to the current in the coil. Eddy currents induced at the surface of a test material are of a certain magnitude and phase, and vary with time. Material properties and discontinuities such as cracks disturb the trajectories of the eddy current and thus affect the magnitude and phase of the induced current. The probe senses the magnetic field induced by currents components of that produce a complex voltage in the coil. The Eddy Current testing method requires that the potential difference across the coil or the changes in changes in impedance are very small, differential measurements are used to impedance be determined. Given that improve the resolution of the signal

## 2.3 Conclusions

In metallic structures, small cracks gradually develop due to cyclic loads and eventually the crack whose stress intensity factor exceeds the fracture toughness leads to catastrophic failure. Stress intensity factor depends on both crack length and applied stress. Thus, inspection techniques both to detect small crack and to evaluate crack length are crucial to secure the reliability of metallic structures.

Cracks in structural materials can be detected in several ways. Optical fibers are useful as strain gauges because their long length makes them amendable to detecting strain over wide areas. Disadvantage of using optical fibers are that they are expensive to incorporate into the metallic structure, and may additionally degrade material integrity. Frequency response methods can be used to detect a change in stiffness of the structure by measuring a shift in natural frequencies when the structure has been damaged. Ultrasonic and X-Radiography are also used to characterize structural materials, but require access to both the front and back of the structure under test as well as the use of bulky equipment. All of these systems require a means to power the sensor and to physically connect to electrical leads to read out sensory information. In many cases, it is preferred that the sensor be built into the structural material with data read out wirelessly. Additionally, it is also preferred that the sensor can be powered wirelessly, eliminating the need for a power source connection or for an imbedded battery.

### 3 CRACK SENSING ELEMENT DESIGN

This chapter starts with the construction of the proposed passive crack sensor and the physical model of the interdigital capacitor as the crack sensing element. After the exploration of the geometry dependent capacitance of the interdigital capacitor, the crack sensing principles of the interdigital electrodes are explained thoroughly. Aiming at minimizing sensor size and optimizing sensor sensitivity, design considerations of the geometric dimensions of the interdigital capacitor are discussed. Meanwhile, the performance of the optimized interdigital capacitor is simulated based on the above consideration.

#### 3.1 Parallel Plate Capacitor

A capacitor is a device that store electric charge. Capacitors vary in shape and size, but the basic configuration is a passive electronic component consisting of a pair of conductors separated by an insulator. When there is a voltage across the conductors a static electric field develops in the dielectric that stores energy and produces a mechanical force between the conductors. An ideal capacitor is characterized by a single constant value, capacitance, measured in farads. This is the ratio of the electric charge on each conductor to the potential difference between them.

For example, if there are two isolated conductive objects of arbitrary shape (plates) and they are connected to the opposite poles of battery. (Figure 3-1) The plates will receive equal amounts of opposite charges;  $q$ .

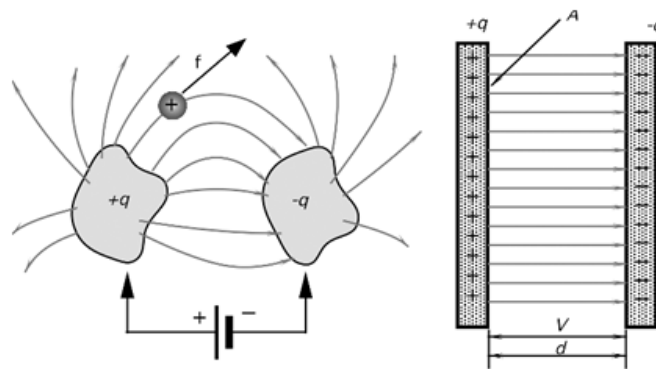
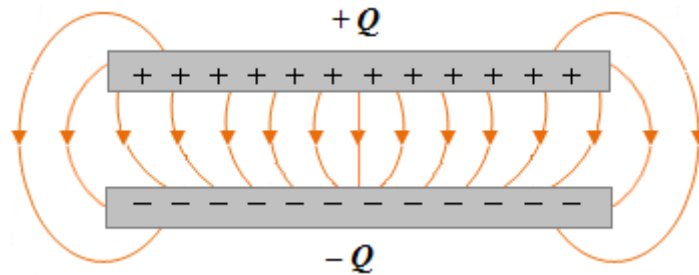


Figure 3-1 A parallel-plate capacitor

To calculate the capacitance, we must relate  $V$ , the potential difference between the plates, to  $q$ , the capacitor charge:

$$C = \frac{q}{V} \quad (3.1)$$

In order to get the expression for the capacitance in systems with simple geometry, let consider two metallic plates of equal area separated by a distance  $d$ , as shown in Figure 3-2. The top plate carries a charge  $+Q$  while the bottom plate carries a charge  $-Q$  [31]



**Figure 3-2 The electric field between the plates of a parallel-plate capacitor**

A real capacitor has a finite size. Thus, the electric field lines at the edge of the plates are not straight lines, and the field is not contained entirely between the plates. This is known as edge effects, and the non-uniform fields near the edge are called the fringing fields. In Figure 3-2 the field lines are drawn by taking into consideration edge effects. However, the field lines between the plates will be considered straight lines for assuming an idealized situation. The electric field between plates can define as:

$$V = \int_0^d E dz = \int_0^d \frac{\rho}{\epsilon} dz = \frac{\rho d}{\epsilon} = \frac{Qd}{\epsilon A} \quad (3.2)$$

Solving this for  $C=Q/V$  reveals that capacitance increase with area and decrease with separation.

$$C = \frac{\epsilon A}{d} \quad (3.3)$$

## 3.2 Interdigital Capacitor

Interdigital capacitor (IDC), one of the most commonly used periodic structures for sensor applications, are widely involved in many advanced applications such as non destructive testing (NDT), microelectromechanical system (MEMS), telecommunication, biosensing, chemical sensing and piezoelectricity. Before we get into the proposed crack sensing principle, an approximation model of interdigital capacitor will be briefly illustrated.

### 3.2.1 IDC analysis model

The operating principle behind the interdigital capacitor is very similar to a parallel plate capacitor. Figure 3-3 shows the relationship between a parallel plate capacitor and an interdigital capacitor, and how the transition occurs. There is an electric field between the positive and negative electrodes and Figure 3-3 (a) and (b) shows how these fields pass through the material under test (MUT). As suggested in Figure 3-3, it is obvious that material dielectric properties as well as the electrode and material geometry affect the capacitance and the conductance between the two electrodes.

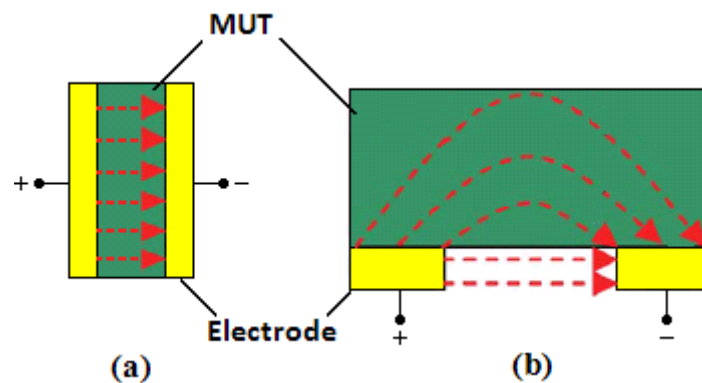


**Figure 3-3 Operating principle of interdigital sensor**

Figure 3-4 shows a layout of the electrode plane and a schematic diagram of the cross-section of an IDC sensor with two interpenetrating comb electrodes. The gaps between electrodes have a width of  $g_c$  while the fingers have a width of  $w_c$ . All the fingers are connected to two common comb electrodes. These two comb electrode

have a number ( $N_C$ ) of fingers of length  $L_C$  and are connected to each end of the spiral inductor.

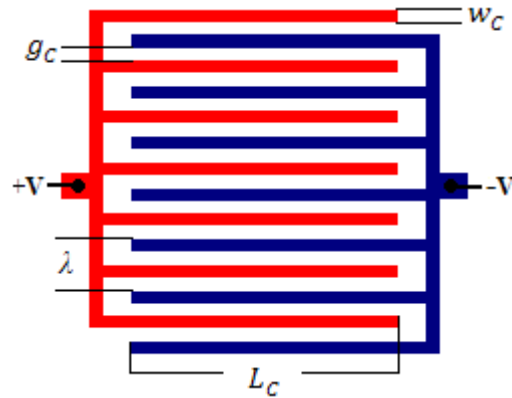


**Figure 3-4 Layout of electrode plane**

The geometric dimensions of a typical IDC are also schematically illustrated in Figure 3-5, this figure shows a 2-dimensional cross-sectional view of the IDC with all the geometric dimensions and dielectric properties notified.

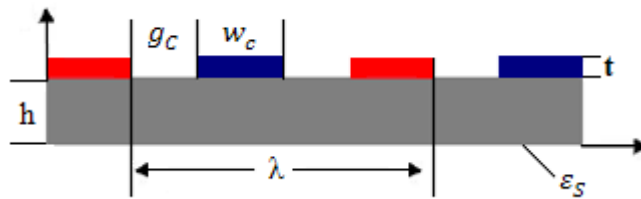


**Figure 3-5 Cross-section of IDC geometric dimensions**

In a geometrically symmetrical capacitor, the perpendicular plane halfway between electrodes is equal-potential planes. In common practice, this plane is considered as an electric ground and its voltage is set to zero. The electric field lines cross normal to this plane as shown in Figure 3-6.

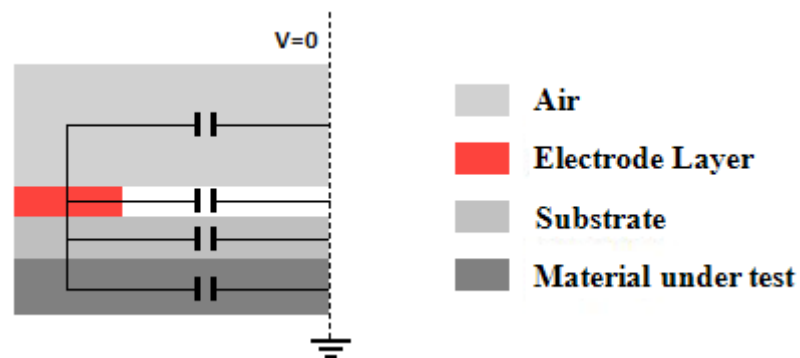


**Figure 3-6 Half unit cell model of the proposed multilayer interdigital capacitor**

This kind of assumption only holds true for an infinite periodic structure whose electrodes fingers have an infinite length. However, in the case of a finite periodic structure, there will be an error incurred by this assumption because the impacts from other cells and the variation in the ground planes cannot ignore. In the vicinity to the electrode boundary, this error will be amplified. Therefore, it is assumed that most of the polarization phenomena occur in a region. As for the finite length of the electrodes a much greater than the wavelength of the IDC structure, for practical purpose, they can be considered as infinity.

In most case, since the thickness of the electrodes is much thinner than their width, the capacitance is specified between the upper and lower half planes of the electrodes by neglecting the capacitance at the side walls. However, the thickness of the electrodes in our design is too thick to be ignored. Corrections to the equations derived by Igreja are added taking into the account of electrode thickness seen in Equations 3.4 and 3.5.

It should be pointed out that in our design, we consider the substrate, which is at the lower half plane of the IDC, is a finite layer because the thickness of the substrate ( $\sim 100\mu\text{m}$ ) is not much smaller than the wavelength of the IDC. Whereas, the specimen is considered as an infinite layer because the thickness of the specimen ( $\sim 5\text{mm}$ ) is much greater than the wavelength. For general practice, in the upper half plane, the air is considered as infinite layers, (Figure 3-6).

The calculation of either the  $C_I$  or  $C_E$  can be done based on this half unit cell model. Where  $C_I$  is the half the capacitance of one interior electrode relative to the ground potential and  $C_E$  is the capacitance of one outer electrode relative to the ground plane next to it. (Figure 3-7)

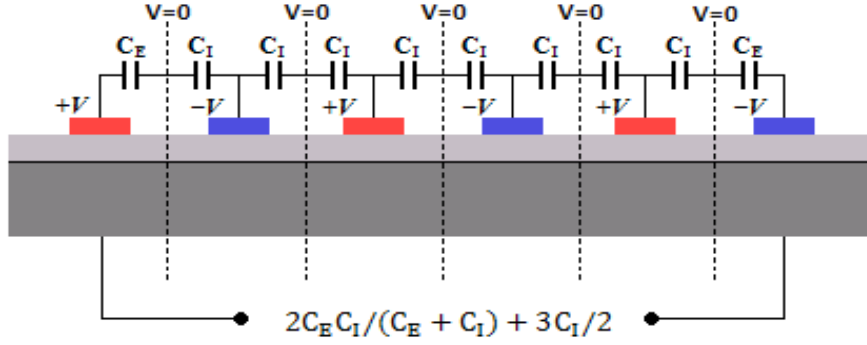


**Figure 3-7 The equivalent circuit of the top air interdigital capacitor**

The total capacitance of the half unit cell  $C_I$  and  $C_E$  can be treated as a summation of three individual capacitances which are given below:

$$C_I = C_{I\_air\infty} + C_{I\_substrate} + C_{I\_steel\infty} \quad (3.4)$$

$$C_E = C_{E\_air\infty} + C_{E\_substrate} + C_{E\_steel\infty} \quad (3.5)$$

Based on the so-called partial capacitance technique, the multilayered structure on the testing material can be split into three individual layers with capacitances shown in Figure 3-7.

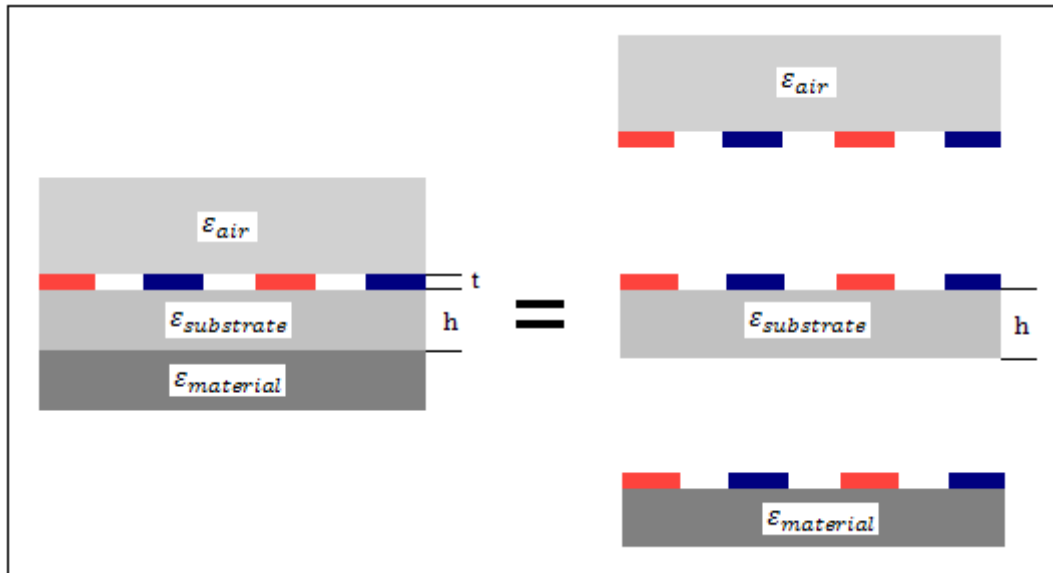


**Figure 3-8 Splitting of the proposed three layered IDC [32]**

The capacitances of the IDC unit cell with infinite layer and finite layer at interior or exterior electrodes are described using a complete elliptic integral of the first kind  $K[k]$ . The detailed calculations are shown in Table 3-1.

**Table 3-1: Detailed equations needed for the calculation of  $C_E$  and  $C_I$ .**

	Interior electrodes	Exterior electrodes
Finite layer	$C_I = \varepsilon_0 \varepsilon_r \frac{K(k_I)}{K(k'_I)}$ $k'_I = \sqrt{1 - k_I^2}$ $k_I = t_2 \sqrt{\frac{t_4^2 - 1}{t_4^2 - t_2^2}}$ $t_2 = \text{sn}(K(k)\eta, k)$ $t_4 = \frac{1}{k}$ $k = \left( \frac{v_2(0, q)}{v_3(0, q)} \right)^2$ $q = \exp(-4\pi r)$	$C_E = \varepsilon_0 \varepsilon_r \frac{K(k_E)}{K(k'_E)}$ $k'_E = \sqrt{1 - k_E^2}$ $k_E = \frac{1}{t_3} \sqrt{\frac{t_4^2 - t_3^2}{t_4^2 - 1}}$ $t_2 = \cosh\left(\frac{\pi(1 - \eta)}{8r}\right)$ $t_4 = \cosh\left(\frac{\pi(1 + \eta)}{8r}\right)$
Infinite layer	$C_I = \varepsilon_0 \varepsilon_r \frac{K(k_{I\infty})}{K(k'_{I\infty})}$ $k_{I\infty} = \sin\left(\frac{\pi}{2}\eta\right)$	$C_E = \varepsilon_0 \varepsilon_r \frac{K(k_{E\infty})}{K(k'_{E\infty})}$ $k_{E\infty} = \frac{2\sqrt{\eta}}{1 + \eta}$

where  $K(k_I)$  is the complete elliptic integral of the first kind with modulus  $k$ ,  $k'$  is the complementary modulus of  $k$ ,  $v_2$  and  $v_3$  are the Elliptic theta functions,  $\text{sn}(z, k)$  is the Jacobi elliptic function of modulus  $k$ ,  $\lambda = 2(g_c + w_c)$  is the spatial wavelength,  $\eta$  is the ratio between the electrode width and the unit cell width which is known as the metal ratio, and  $r$  is the ratio between the thickness of each layer and the spatial wavelength.  $\eta$  and  $r$  are two geometric dimensional parameters.

The total capacitance of the IDC with  $N_c$  fingers of length  $L_C$  is given as

$$C = (N_c - 3) \frac{C_{I,IDC}}{2} + 2 \frac{C_{I,IDC} C_{E,IDC}}{C_{I,IDC} + C_{E,IDC}}, \quad N > 3 \quad (3.6)$$

As noticed in Equation 3.6 and Table 3.1, the capacitance of the interdigital capacitor is a function of  $\eta$  and  $r$ , the thickness, length and number of electrodes, and as well as the dielectric permittivity of each layer  $\varepsilon_r$ .

$$C = C(\eta; r; \varepsilon_S; \varepsilon_{steel}; h; t; L_C; N_C) \quad (3.7)$$

Where  $C_{I,IDC}$  and  $C_{E,IDC}$  are developed using the equations and the partial capacitance technique [32]. A IDC sensor with a thick substrate of relative permittivity  $\epsilon_s$ , top air layer of relative permittivity  $\epsilon_I$  and the infinite material layer of relative permittivity  $\epsilon_{steel}$  will have their total capacitance  $C_{I,IDC}$  (Interior electrodes capacitance) and  $C_{E,IDC}$  (Exterior electrodes capacitance) given by:

$$C_{I,IDC} = C_{I\_air\infty} + C_{I\_substrate} + C_{I\_steel\infty} \quad (3.8)$$

$$C_{E,IDC} = C_{E\_air\infty} + C_{E\_substrate} + C_{E\_steel\infty} \quad (3.9)$$

Using the connotation shown in Figure 3-8 and equation 3.4 and 3.5 we have:

$$C_{I,IDC} = \epsilon_0 L_C \left[ \frac{K(k_{air\infty})}{K(k'_{air\infty})} + \epsilon_{steel} \frac{K(k_{I,S\infty})}{K(k'_{I,S\infty})} + (\epsilon_s - \epsilon_{steel}) \frac{K(k_{I,S\infty})}{K(k'_{I,S\infty})} \right] \quad (3.10)$$

$$C_{E,IDC} = \epsilon_0 L_C \left[ \frac{K(k_{air\infty})}{K(k'_{air\infty})} + \epsilon_{steel} \frac{K(k_{E,S\infty})}{K(k'_{E,S\infty})} + (\epsilon_s - \epsilon_{steel}) \frac{K(k_{E,S\infty})}{K(k'_{E,S\infty})} \right] \quad (3.11)$$

This 2-D unit provide us a simplified model which enable us to give a reasonable analysis on real IDC cell for its variation of the capacitance with respect to the geometry design (section 3.2.2), the crack extension (section 3.2.3).

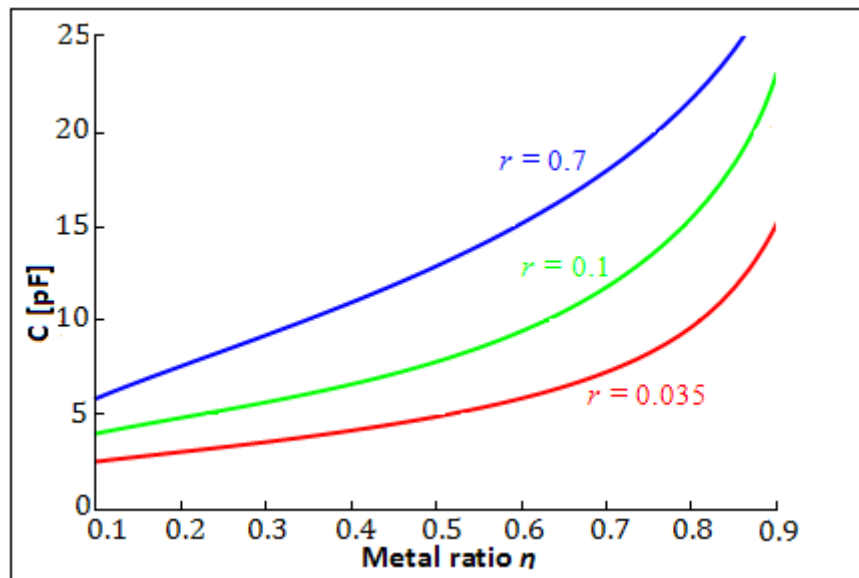
### 3.3 Geometry Dependent Capacitance

As noticed in Equation 3.7, the impact of geometry on the capacitance of IDC cell manifests on the parameter such as  $N_C$ ,  $L_C$ ,  $\eta$  and  $r$ . Therefore the dependence of capacitance on these four parameters has been studied.

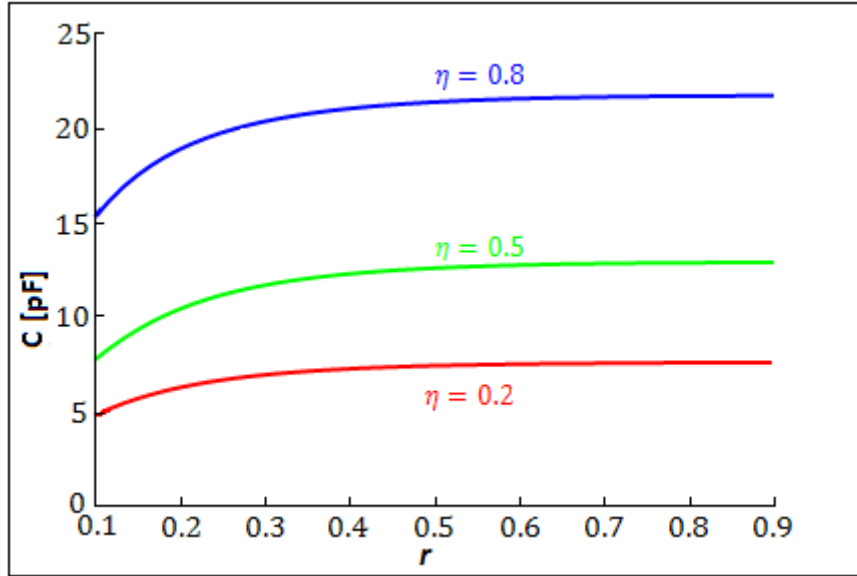
In this study, the discussed range of parameters  $\eta$  and  $r$  are, from 0.01 to 0.99 and from 0.05 to 0.95, respectively. Other parameters are set as follows:  $\epsilon_s = 3.9$  and  $N_C = 26$ ,  $L_C = 23\text{mm}$ . Representative calculated capacitances with respect to each selected  $\eta$  are plotted in Figure 3-9 (a). In the case of metal ratio  $\eta = 0.2$ , the unit cell has a wide gap and narrow finger. On the other hand, in the case of metal ratio  $\eta = 0.8$ , the unit cell has a narrow gap and wide finger. As can be seen in the Figure 3-9 (a) the capacitance of the former IDC unit is much smaller than the latter IDC unit. The capacitance of IDC unit increases smoothly and exponentially with the increasing value of metal ratio  $\eta$ .

The calculated capacitance of an IDC at a fixed metal ratio with respect to  $r$  is shown in Figure 3-9 (b). The unit cell length in our simulation is set as constant. In the range from 0 to 0.35 of  $r$ , the increasing substrate thickness leads to the increase of the capacitance and the capacitance reaches a maximum value at  $r = 0.35$ . Then there is not significant increase anymore with further increasing the value of  $r$ . For decreasing metal ratio  $\eta$ , the capacitance decreases exponentially.

Close inspection of the Figure 3-9 (a) and (b) suggest that when  $r$  is greater than 0.4 the calculated capacitance of IDC unit cell is relatively insensitive of value of  $r$ , dependent only on the metal ratio  $\eta$ . More interestingly, the capacitance increase exponentially when the value of metal ratio  $\eta$  is close to 0.9. Therefore, for the practical purpose the best choice of the geometry of IDC unit is that,  $r$  is not less than 0.4, and  $\eta$  is as close as possible to 0.9. However, as noticed in the range 0.8-0.9 of  $\eta$  the change of capacitance is nonlinear. Thus, in order to have a better sensing linearity, in real design, we are trying to avoid this range.



(a)

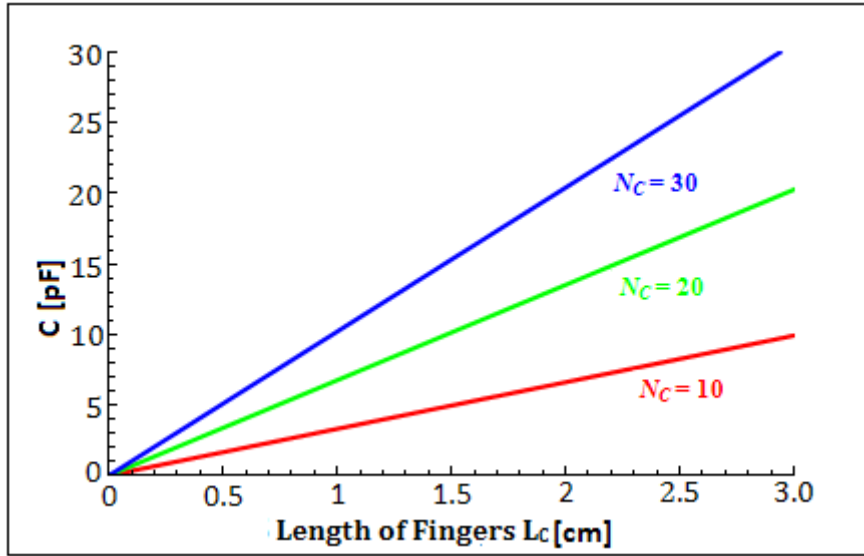


(b)

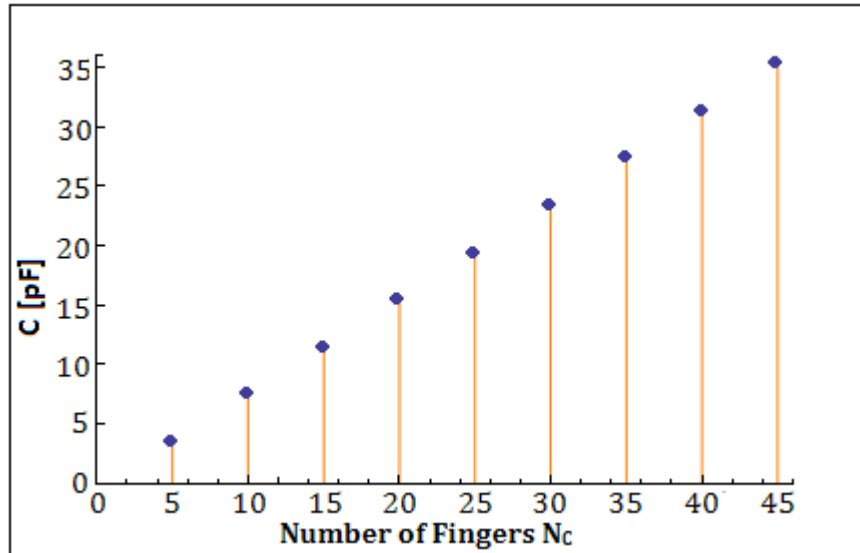
**Figure 3-9 Capacitance as a function of  $\eta$  and  $r$**

Based on above analysis to achieve a larger range of capacitance and greater sensitivity, it is desirable that the IDC incorporate a small unit cell with a big metal ratio. Moreover, to get a stable capacitance that is not influenced by the substrate, the thickness of the substrate must be bigger than 40% of the unit cell length. However, the variation in  $r$  can also be utilized in the crack sensing, this is because the thickness of each layer is slightly changed during the deformation. In this case, an  $r$ , which is smaller than 0.4, is desired.

In this study, range of parameters  $L_C$  and  $N_C$  are, from 0 to 30mm and from 5 to 45. Other parameters are set as follows:  $\epsilon_s = 3.9$  and  $r = 1/26$ ;  $\eta = 0.38$ . Representative calculated capacitances with respect to each selected  $N_C$  are plotted in Figure 3-8 (a) and (b).



(a)



(b)

**Figure 3-10 Capacitance as a function of  $L_c$  and  $N_c$**

The calculated capacitance of an IDC at a fixed  $N_c$  with respect to  $L_c$  is shown in Figure 3-10 (a) that. In the selected  $N_c$  for 10, 20 and 30, the increasing number of electrodes increases the capacitance and the capacitance reaches a maximum value at  $N_c=30$ . In case of decreasing  $N_c$ , the capacitance decreases linearly at a high slope. Close inspection of the Figure 3-10 (a) and (b) suggest that the capacitance of IDC sensor increases linearly with the increasing both of  $L_c$  and  $N_c$ .

### 3.4 Crack Dependent Capacitance

According to our design, the capacitance value of IDC sensor changes when the crack occurs and propagates in the MUT. This capacitance variation depends on the crack initial position, orientation and the crack length.

#### 3.4.1 Crack parameters in IDC sensor

First, we give a basic definition for IDC Sensor parameter and the crack parameter, as denoted in the Figure 3-12.

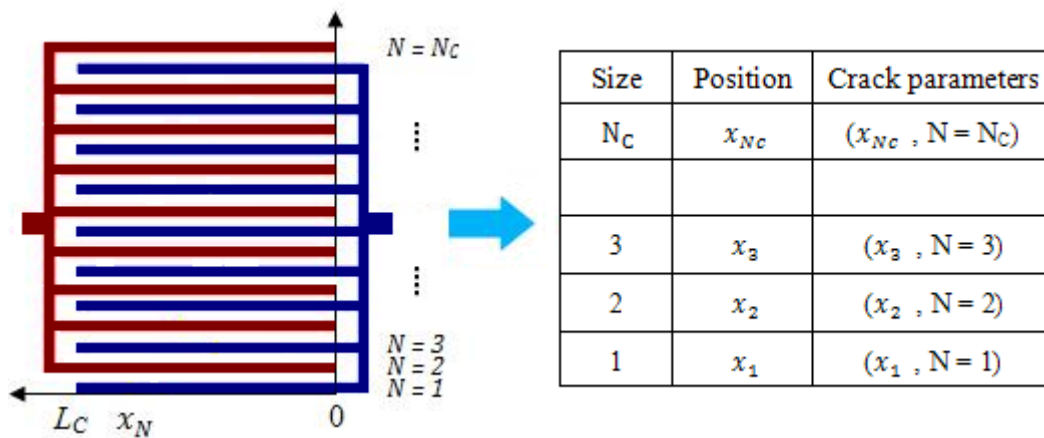


**Figure 3-11 Parameter of IDC sensor**

As shown in Figure 3-11,  $N$  is a parameter vital to crack size, which means the number of fingers been broken during the crack propagation. Another parameter  $x_N$  is defined as crack position according to different crack size  $N$ .

#### 3.4.2 Crack angle definition

Crack propagation angle is the parameter which manifests the crack orientation. The expression of crack angle between the two neighboring fingers  $N$  and  $N+1$  is  $\theta_{[N,N+1]}$ . Figure 3-12 depicts the crack angle  $\theta_{[N,N+1]}$  between the different units IDC.

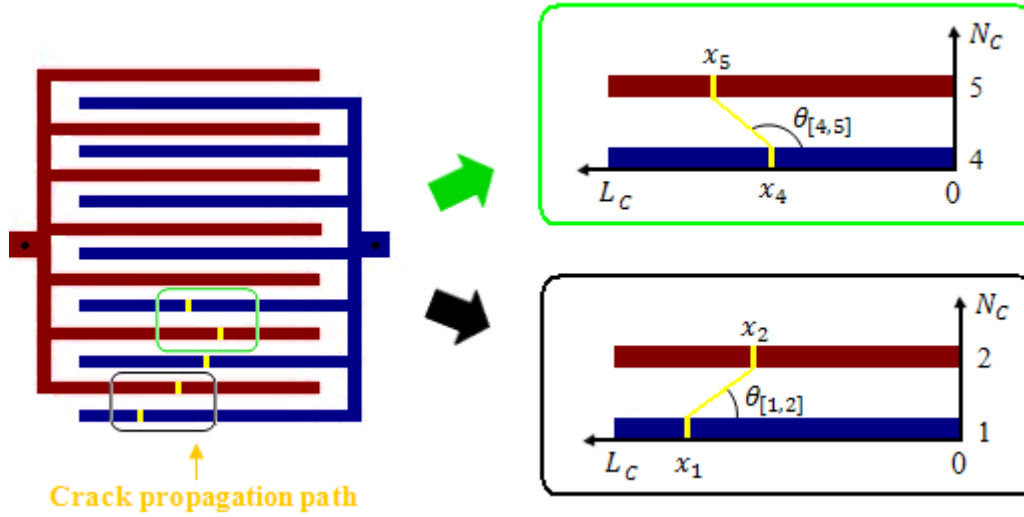


**Figure 3-12 Crack orientation**

As shown in Figure 3-13, depend on the different crack size  $N$  and crack position  $x_N$ , the crack angle  $\theta_{[N,N+1]}$  can be calculated by equation 3-12 and equation 3-13.

$$\theta_{[N,N+1]} = \pi - \tan^{-1} \frac{g_c}{x_N - x_{N+1}}, \text{ when } \theta \geq 90^\circ \quad (3.12)$$

$$\theta_{[N,N+1]} = \tan^{-1} \frac{g_c}{x_{N+1} - x_N}, \text{ when } \theta \leq 90^\circ \quad (3.13)$$

### 3.4.3 Crack length definition

Crack length  $l$  is another important parameter to identify the crack propagation path. Unit crack length between each two neighboring fingers is varied during the crack propagation. In order to get the total crack length information,  $l_i$  is definite as the unit crack length between the two neighboring fingers. The simulation of the unit crack length is denoted in the Figure 3-14.

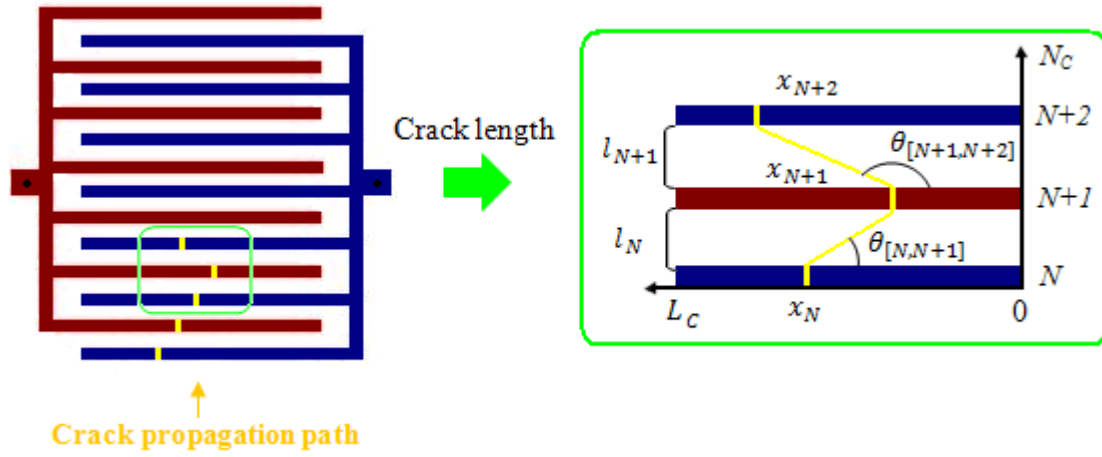


**Figure 3-13 Unit crack length simulation**

Total crack length  $l$  is the summation for all the unit crack length  $l_i$ . Assume the crack size is  $N$ , the total crack length can be calculated by equation 3-14.

$$l = \sum_{i=1}^{N-1} l_i = \sum_{i=1}^{N-1} \frac{g_c}{\sin \theta_{[i,i+1]}} \quad (3.14)$$

In order to investigate the crack dependent capacitance of IDC, some reasonable crack configurations are applied to the test coupon as listed in Table 3-2.

**Table 3-2: Electrical Parameter Values**

Design Parameter	Symbols	Value
The number of total electrodes	$N_C$	26
The length of each fingers	$L_C$	23mm
Thickness of fingers	$t$	35um
Thickness of substrate	$h$	100um
The width of each fingers	$w_C$	500um
The gaps width between electrodes	$g_C$	800um

The choice of parameter calculation reflects the configuration of demonstration test of prototype sensor. Major discussion shall be outlined as follows.

### 3.4.4 Discussion

#### Initial location of crack

It is vital to locate the point where the crack initiates. Here we start with the case where crack forms at the first finger electrode. Assume the crack forming at a different initial position  $x_1$  ( $0 \leq x_1 \leq L_c$ ). In this case, the capacitance of IDC sensor is varied as the position  $x_1$ , which is indicated in Figure 3-14.

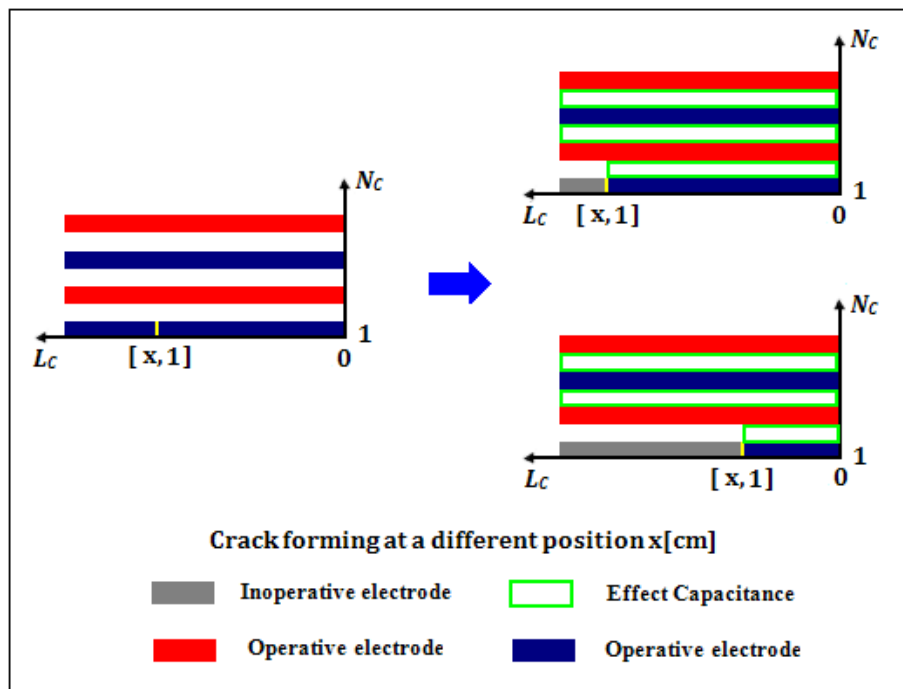


Figure 3-14 Arbitrary crack initial location  $x_1$

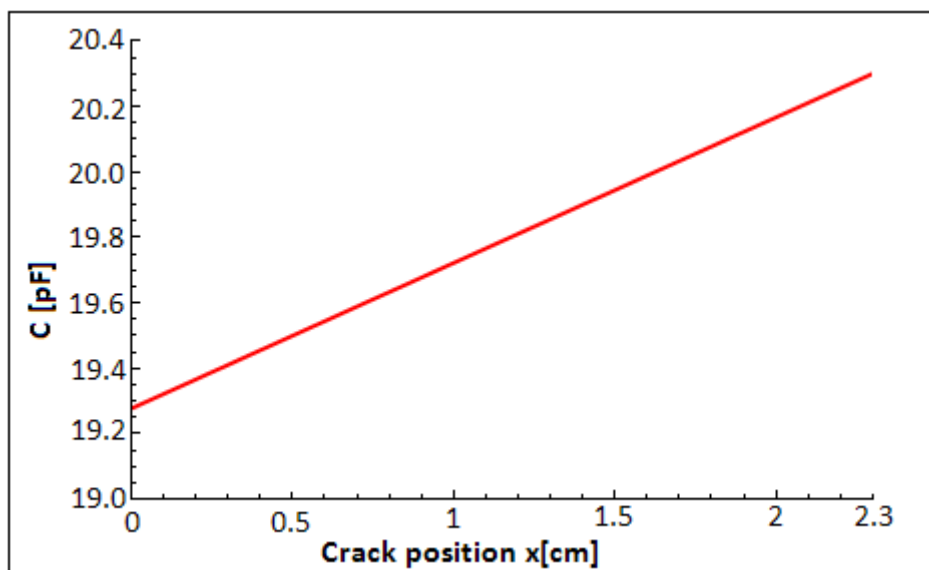


Figure 3-15 IDC capacitances vs. Arbitrary crack initial position  $x_1$

The linear shown in Figure 3-15 dependence of IDC capacitance on the position of  $x$  suggests that provided the sensitivity of sensor is high enough, we can determine locate the exact position where crack occurs.

*Orientation of crack*

When the crack initiates, after the consumption of many cycles, the crack may change in direction when the maximum principal normal stress governs crack growth. It is vital to determine the crack orientation angle during the crack growth.

Here we discuss with the case between first two neighboring fingers. Assume the crack forms at  $x_1$  and elongate at an arbitrary angle  $\theta$  ( $0^\circ$  to  $180^\circ$ ). In this case, the capacitance  $C_s$  is varied as a function of crack propagating angle  $\theta$  and the initiation position  $x_1$  which is shown in Figure 3-16. The Figure 3-17 depicts the relationship between the calculated capacitance and crack propagating angle  $\theta$ .

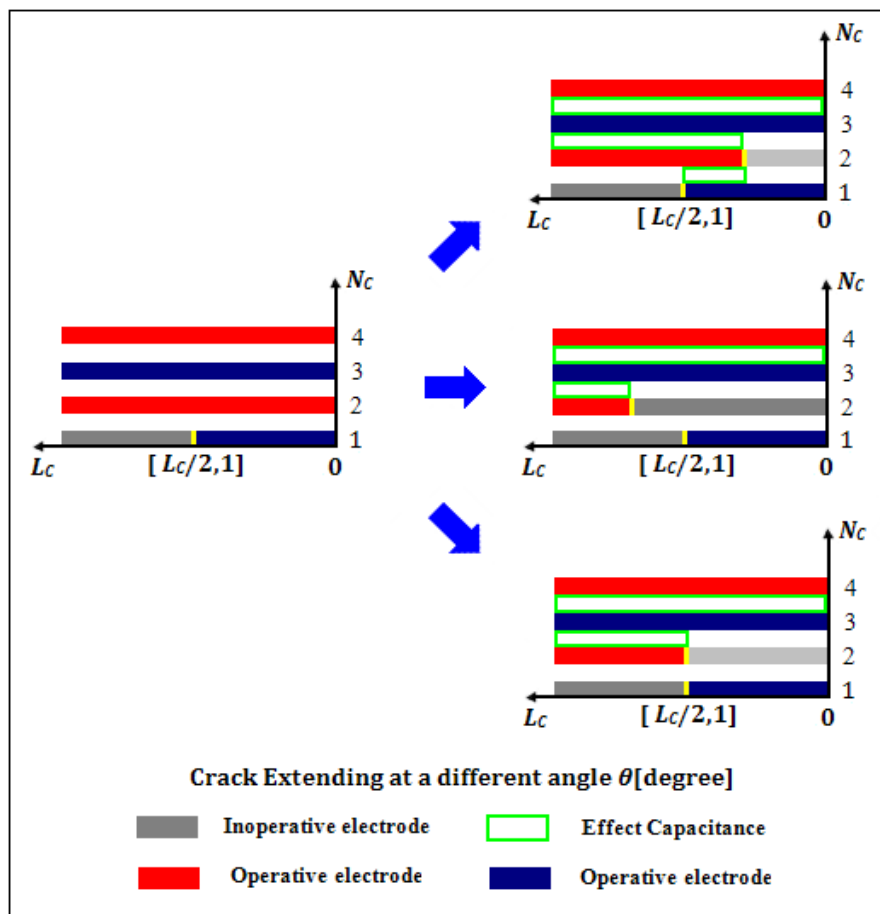
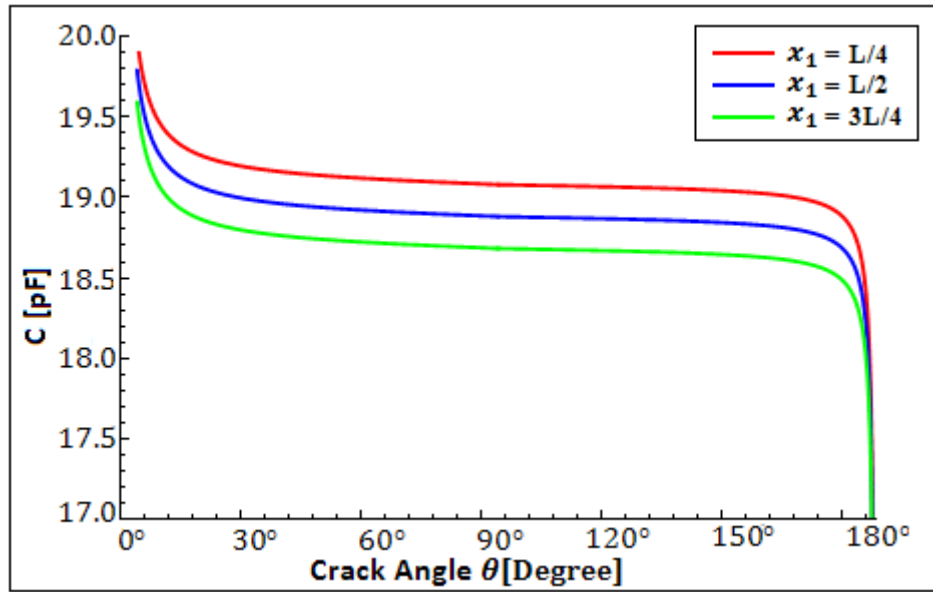


Figure 3-16 Different crack initial position  $x_1$  and arbitrary crack propagation angle  $\theta$



**Figure 3-17 IDC capacitances vs. different crack initial position  $x_1$  and arbitrary crack propagation angle  $\theta$**

As shown in the Figure 3-17, the IDC capacitance decreases exponentially when the crack propagate at the range of  $0^\circ - 30^\circ$  and  $150^\circ - 180^\circ$  degrees. However, there is not significant decrease with the crack propagate angle between  $30^\circ - 150^\circ$  degrees, by consider with the inductor of the antenna and improve the IDC sensor's performance, we can still identify the crack propagate angle due to the capacitance change of the IDC sensor. Moreover, the different crack initial position leads to the different calculated capacitance.

In order to obtain the relationship between the calculated capacitance and crack initial position, here we give some particular value for propagating angel  $\theta$ .

Assume the crack forms at an arbitrary position  $x_1$  but propagates at the certain angle  $\theta$  ( $30^\circ$ ,  $60^\circ$ ,  $90^\circ$ ,  $120^\circ$ , and  $150^\circ$ ), which is indicated in Figure 3-18.

The Figure 3-19 depicts the relationship between the calculated capacitance with crack forming position at certain propagate crack angle  $\theta$ .

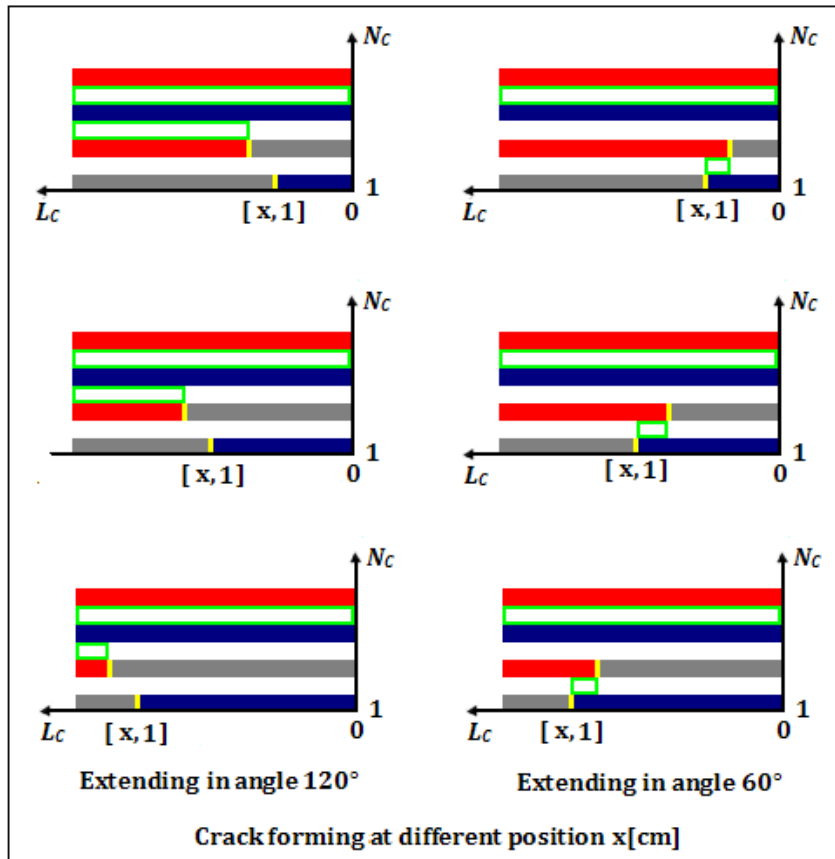


Figure 3-18 Arbitrary crack initial position  $x_1$  and propagate at certain angle  $\theta$

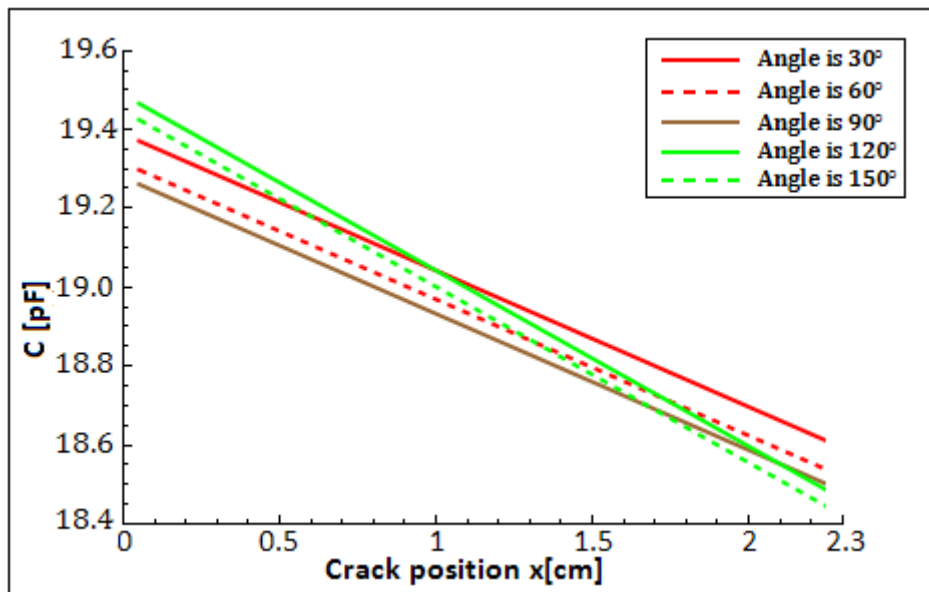


Figure 3-19 IDC capacitances vs. arbitrary crack initial position  $x_1$  and certain crack propagation angle  $\theta$

Close inspection of the Figure 3-17 and Figure 3-19 suggest that when crack initiates and grows at different angle, the calculated capacitance of IDC sensor is sensitive to crack initiation position and propagation angle.

### Crack propagation

The final stage (III) of fatigue fracture is caused by a dynamic crack propagation mechanism. When the crack reaches a critical length and consequently, crack propagation occurs very rapidly. For this reason it is important to measure the length of the crack before fracture occurs.

For the case that the crack size is reaches  $N=4$  to identify how the capacitance varied due to the larger crack length.

Assume the crack forms at  $x_1$  and propagates at an arbitrary angle  $\theta$  ( $0^\circ$  to  $180^\circ$ ). In this case, the capacitance  $C_S$  is varied as a function of crack propagating angle  $\theta$ , the initiation position  $x_1$  and also the crack size  $N$ . which is shown in Figure 3-20.

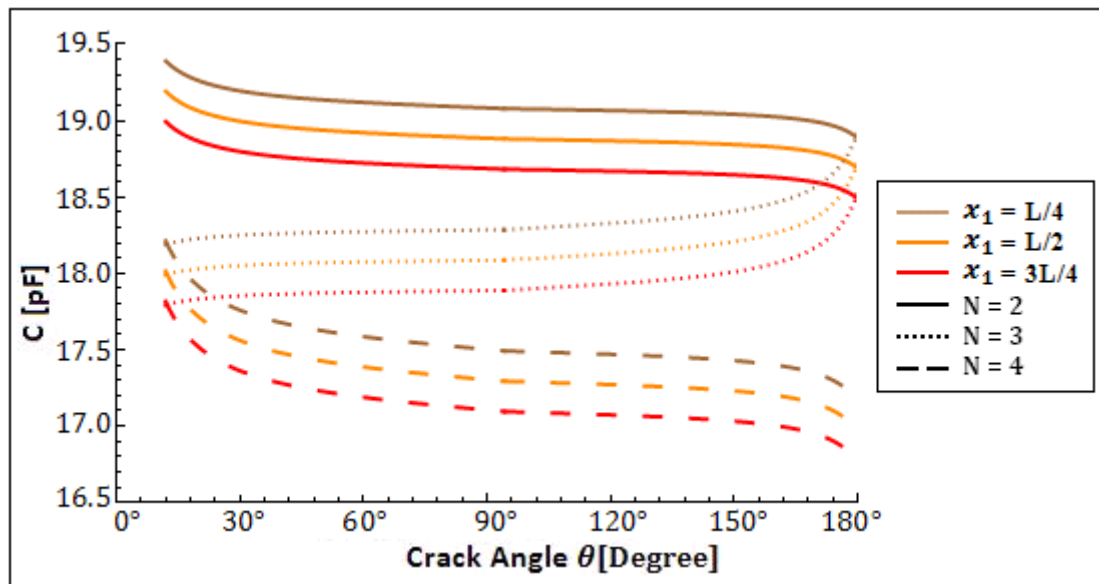
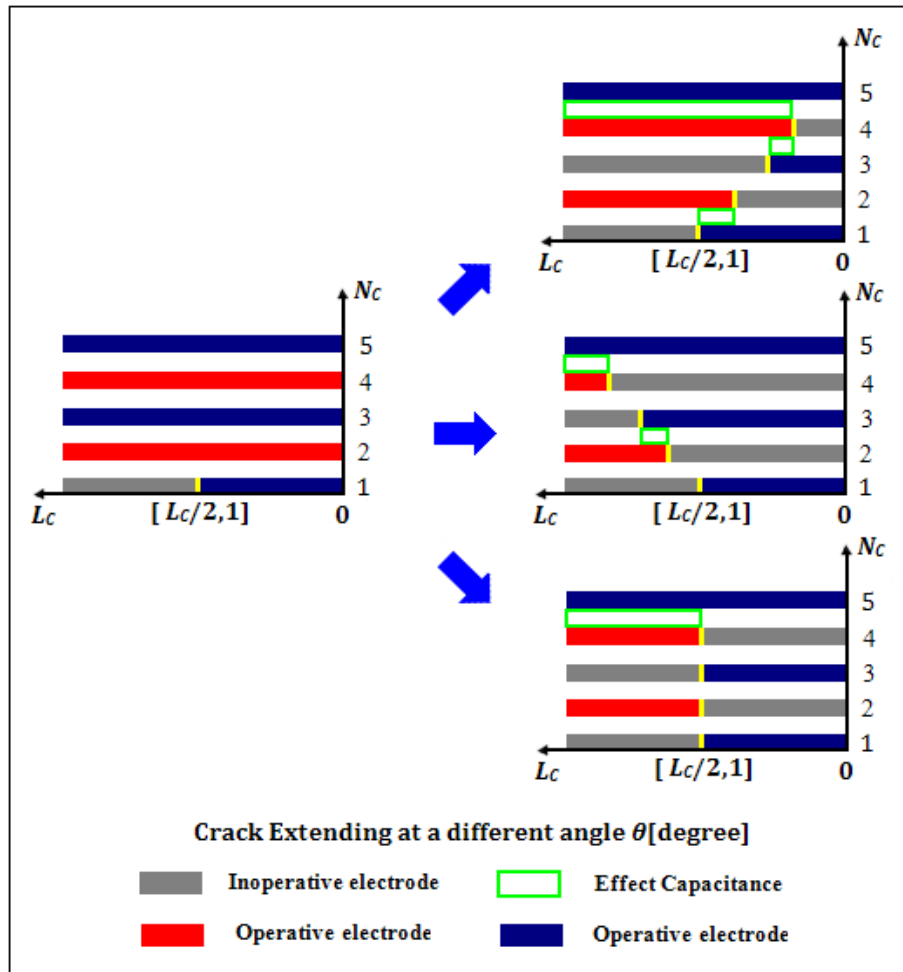


Figure 3-20 IDC capacitances vs. different crack initial position  $x_1$  and arbitrary crack propagation angle  $\theta$  ( $N=4$ )



**Figure 3-21 Different crack initial position  $x_1$  and arbitrary crack propagation angle  $\theta$**

The plot in Figure 3-21 has shown the sensitivity of IDC sensor for the crack length. As the crack elongate, the calculated capacitance decreases. This provide that the IDC sensor has sensitivity to the crack length elongation.

2. In a more general scenario, we assume that crack forms at a different position  $x_1$  and propagate at selected angle  $\theta$  ( $45^\circ$ ,  $90^\circ$ ,  $135^\circ$ ).

The calculated capacitance of IDC at a fixed angle  $\theta$  ( $45^\circ$ ,  $90^\circ$ , and  $135^\circ$ ), which respect for the different initial position  $x_1$  is shown in Figure 3-22(a), (b) and (c).

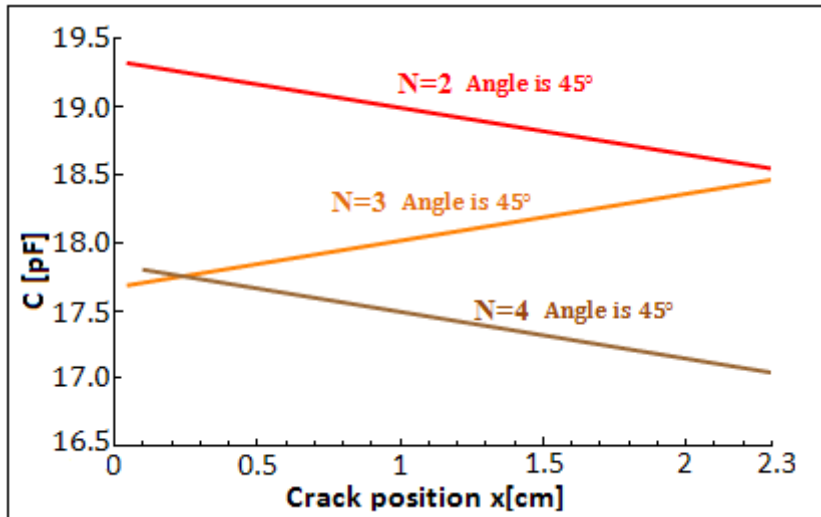


Figure 3-22(a) IDC capacitances vs. different crack initial position  $x_1$  and the crack propagate at angle of  $45^\circ$  for different crack size N

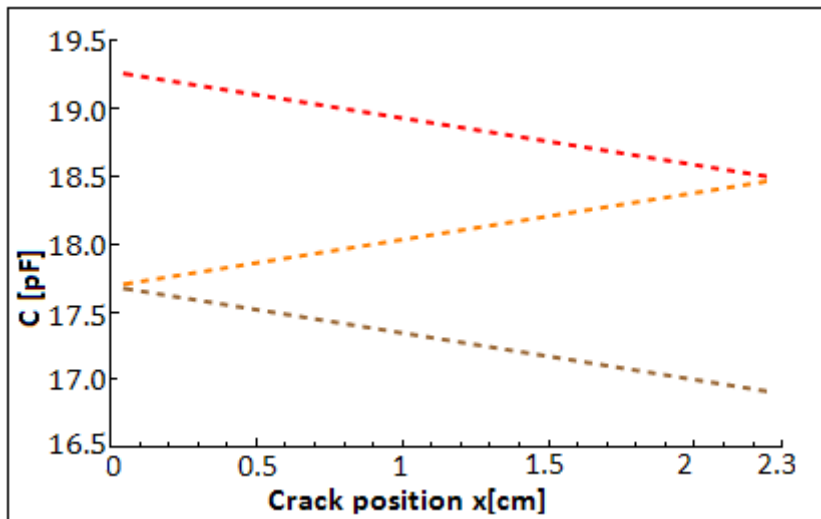


Figure 3-22(b) IDC capacitances vs. different crack initial position  $x_1$  and the crack propagate at angle of  $90^\circ$  for different crack size N

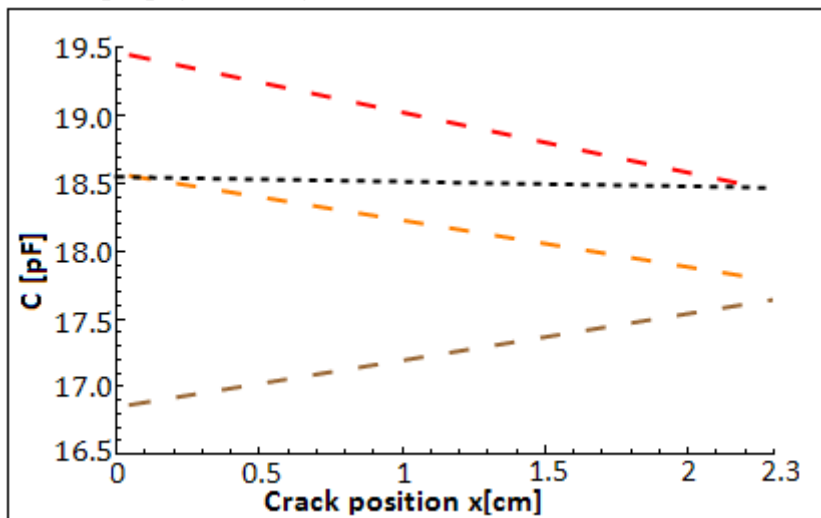


Figure 3-22(c) IDC capacitances vs. different crack initial position  $x_1$  and the crack propagate at angle of  $135^\circ$  for different crack size N

Figure 3-23(a), (b) and (c) depicts that for different crack size ( $N$ ), the calculated capacitance of IDC at a fixed angle  $\theta$  ( $45^\circ$ ,  $90^\circ$ , and  $135^\circ$ ) respect for the different initial position  $x$ .

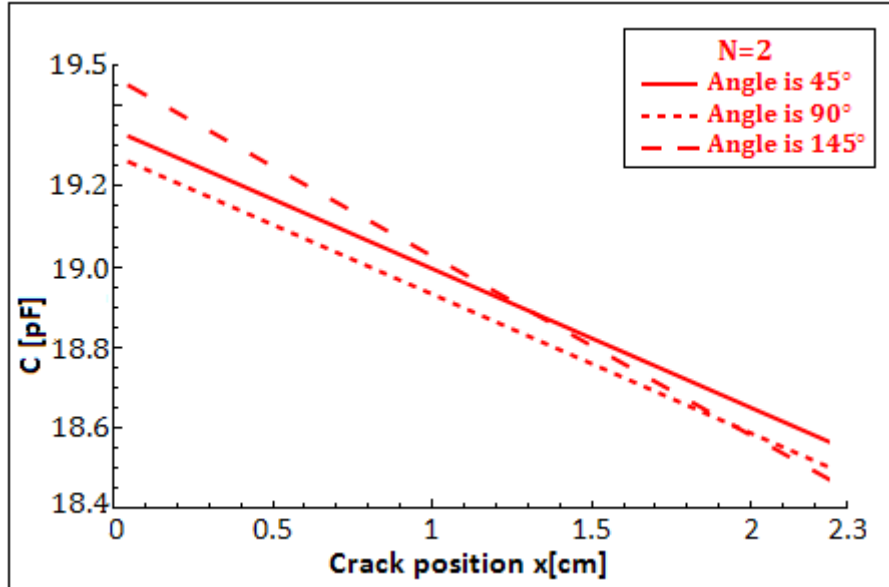


Figure 3-23(a) IDC capacitances vs. different crack initial position  $x_1$  and different crack propagation angle for crack size  $N = 2$

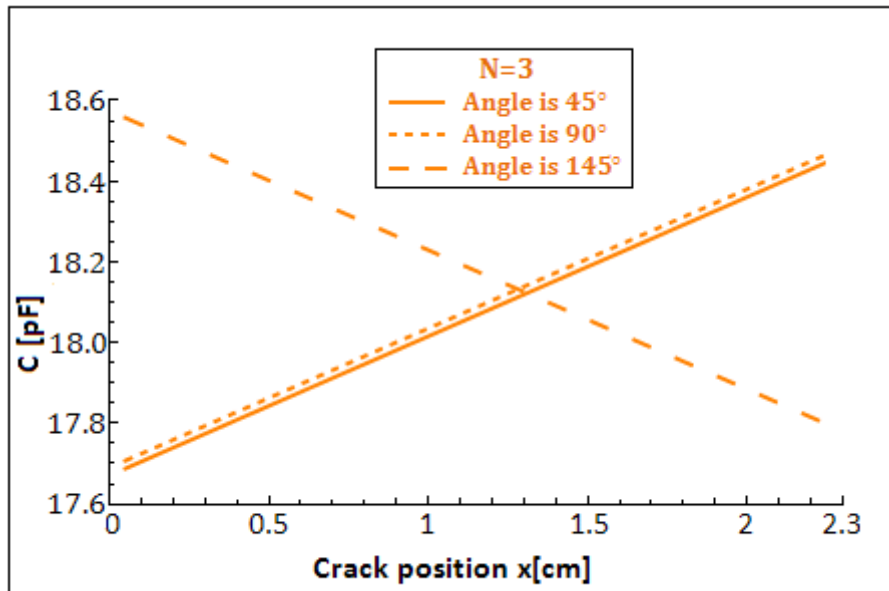
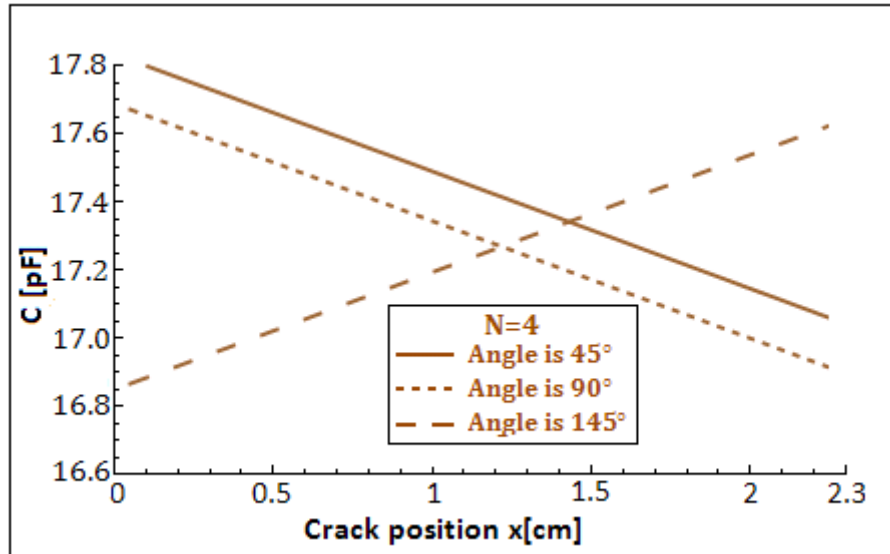


Figure 3-23(b) IDC capacitances vs. different crack initial position  $x_1$  and different crack propagation angle for crack size  $N = 3$



**Figure 3-23(c) IDC capacitances vs. different crack initial position  $x_1$  and different crack propagation angle for crack size  $N = 4$**

All the computer simulations are carried out in MATHEMATICA. Since the special functions in this study are easy to solve in MATHEMATICA, which is a fully integrated software environment for technical and scientific computing.

It is shown in Figure 3-14 that when the crack forms at the different initial position, the capacitance of IDC sensor decreases extent. This simulation result illustrated that the IDC crack sensor has difference crack sensitivity respect to the different crack position.

Close inspection of the Figures 3-18 and Figure 3-19 reveals when the crack propagating in the different angle or forming at different position in neighboring two fingers, the calculated capacitance varies differently. This is suggested the IDC crack sensor has different sensitivity for different relative angles and position between two neighboring fingers. This suggests that the proposed IDC crack sensor should be able to distinguish the crack propagating angle and position between two neighboring fingers in discussed situations.

As the crack elongate ( $N$  is increasing), the calculated capacitance decreases. Moreover, as shown in Figure 3-21, Figure 3-23 and Figure 3-24, the bigger crack size will lead to the smaller calculated capacitance.

More interestingly, for each  $N$  (Number of broken electrode), when the crack form at an arbitrary position  $x$  but propagate at a different angle  $\theta$ , the variation rate of IDC capacitance is considerably different. It is depicted in Figure 3-24(a), (b) and (c).

### **3.5 Conclusions**

In this chapter, the principle of an interdigital capacitor and an IDC model for capacitance analysis are presented. For the purpose of accurate description of crack propagation, the necessary geometry parameters for crack size characterization was defined. In order to achieve a larger range of capacitance and greater sensitivity, the geometry design of the sensor consideration is discussed. Based on the IDC analysis model, a possible crack formation and propagation pattern was proposed. And relationship of crack propagation and resulted capacitance variation has been established by simulation. A sensor prototype was fabricated based on these design considerations.

## 4 SENSOR ANTENNA DESIGN

In this chapter, we will first discuss the concept of construction of the proposed spiral inductor, which is the sensor antenna element. We give a fairly detailed analysis of the geometry dependence of the inductance of the spiral inductor. Moreover, some key parameter such as Q-factor, and coupling factor, which will impact sensor's performance will be discussed.

### 4.1 Spiral Inductor

Since spiral inductors provide high quality factor elements and are feasible in harsh environment applications, they are widely utilized to make resonant circuit elements for capacitive sensors in the microelectronics field. (Figure 4-1)

The spiral inductor acts as a transformer based on the principle of electromagnetic induction, which is illustrated in Figure 1-2. When an oscillating current is executed on the antenna, an alternating voltage at the certain frequency is induced in the spiral inductor based on the changing magnetic field through both the primary antenna and the spiral inductor. The crack formation and extension will induce the change of capacitance, in turn the resonant frequency of LC loop. This change can be detected from reader side by monitoring the impedance across the terminals of the wide bandwidth reader antenna. In other words, the electrical energy is transferred to the sensor from the input antenna, and in the meantime, the crack information can be detected by the reader from the coupled magnetic field.

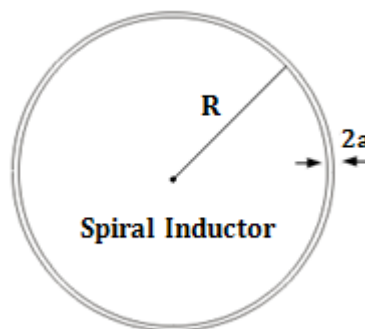


Figure 4-1 Schematic View of Spiral Inductor

In order to read out the crack information, it is essential to design and fabricate an appropriate spiral inductor to have both a reasonable inductance and quality factor. Inductance is the property in an electrical circuit where a change in the electric current through that circuit induces an electromotive force that opposes the change in current. Strictly speaking, this quantity is called self-inductance, because the magnetic field is created solely by the conductor that carries the current. The self-inductance of a straight conductor of length,  $l$ , and radius,  $a$ , (neglecting the effects of nearby conductors), is given by [33]:

$$L \approx \frac{\mu_0 l}{2\pi} \left[ \ln\left(\frac{2l}{a}\right) - 0.75 \right] \quad (4.1)$$

Here the magnetic permeability of free space,  $\mu_0$ , is  $4\pi \times 10^{-7}$  H/m. Different types of spiral inductors have respective calculation equations according to [44]. However, there is no closed-form solution for the inductance of circular loops. The self-inductance of a circular loop of round wire, as shown in Figure 4-1 has a low frequency inductance that can be estimated according to equation 4-2 [33]:

$$L \approx n^2 \mu_0 R \left[ \ln\left(\frac{8R}{a}\right) - 1.75 \right] \quad (4.2)$$

Here the loop radius is  $R$ , the wire radius is  $a$ , and  $n$  corresponds to the turns of the inductor. Figure 4-2 indicates how the coil turn and inductor radius affect inductance, for a wire radius  $a$  of 0.337mm.

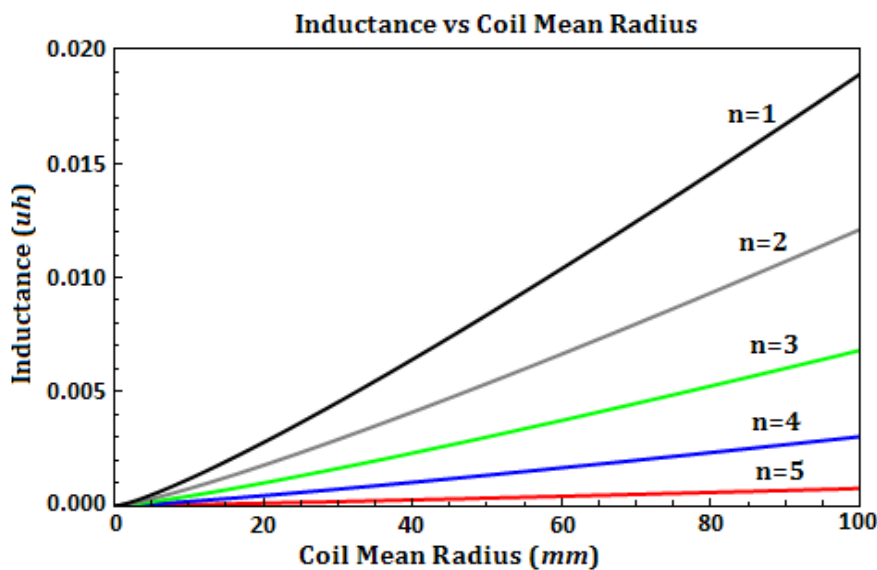


Figure 4-2 Inductance vs. Coil Mean Radius

## 4.2 Coupling Factor

The grade of coupling is expressed by the coupling factor  $k$ . The coupling factor is determined by the distance between the inductors and their relative size. It is further determined by the shape of the coils and the angle between them. If the coils are axially aligned, a displacement causes a decrease of  $k$ . Higher coupling factor  $k$  indicates the more flux reaches the receiver, which means the better the coils are coupled.

A fair approximation of coupling factor  $k$  with respect to design parameter of the proposed sensor in this study is given by equation 4-3

$$k(d) = \left( \frac{r_s r_R}{d^2 + r_R^2} \right)^{\frac{3}{2}} \quad (4.3)$$

However, this only applies if the  $r_R$  fulfill the condition  $r_R \geq r_s$ . Here,  $r_R$  corresponds to the radius of the primary coil,  $r_s$  indicates the radius of the sensor inductor, and  $d$  is the coupling distance [37].

Figure 4-3 illustrates how  $r_s$  and  $d$  affect the coupling factor,  $k$ , when  $r_R = 2.7\text{cm}$ . The plot indicates that minimizing the coupling distance will improve the coupling factor.

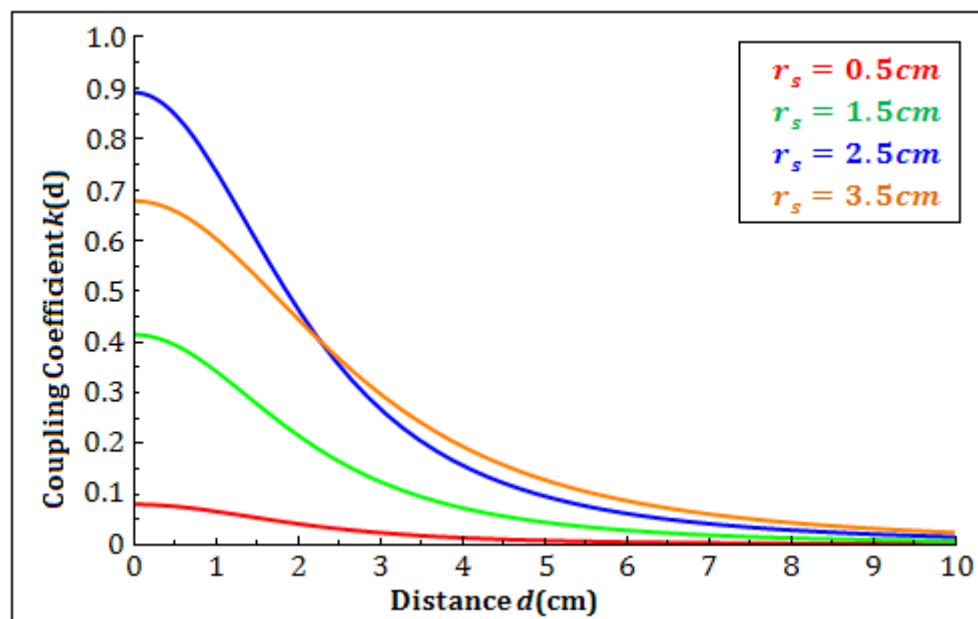
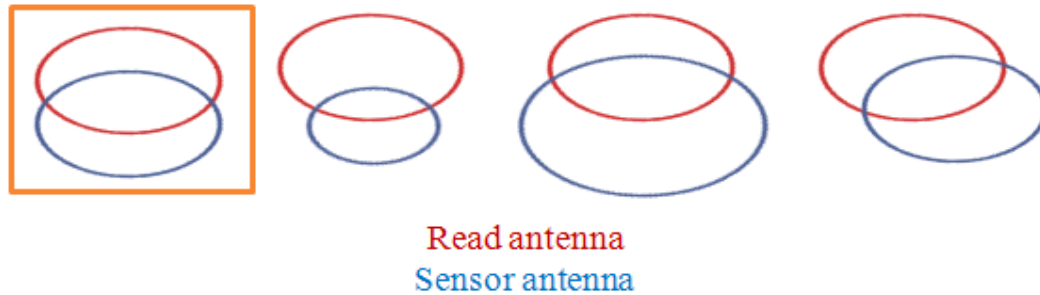


Figure 4-3 Coupling coefficient  $k$  vs.  $d$  and  $R_s$

Close inspection of the Figure 4-4 suggests that when the radius of the sensor inductor  $r_s$  is equal to the radius of the reader antenna  $r_R$ , we will get the maximum coupling factor  $k$ .



**Figure 4-4 Radius of the sensor inductor design result**

### 4.3 Q-factor

The quality of the LC resonant circuit can be evaluated by Q-factor. Higher Q-factor indicates a lower rate of energy loss relative to the stored energy of the LC resonant circuit. And Q-factor also means narrower bandwidth, which is desirable in many applications. In general, the Q-factor is the ratio of the power stored to power dissipated in the circuit reactance and resistance.

$$Q = \frac{P_{stored}}{P_{dissipated}} \quad (4.4)$$

Also the Q-factor can be defined as the ratio of the total stored energy to dissipated energy per unit cycle in this equation:

$$Q = \frac{W_{total}}{P/2\pi f} = \frac{2\pi f W_{total}}{P} \quad (4.5)$$

Here,  $W$  means total stored energy,  $P$  is the average dissipated power, and  $f$  is the resonant frequency.

In order to exhibit a large amplitude response, low internal losses and weak coupling to the external environment are also required. A higher Q-factor indicates a lower rate of energy dissipation relative to the oscillation frequency. Generally, the

$Q$ -factor is interpreted as an indication of the sharpness of the resonance peak. The simplified expression of  $Q$ -factor is defined by:

$$Q = \frac{2\pi f_r L_S}{R_L} = \frac{1}{R_L} \sqrt{\frac{L_S}{C_S}} \quad (4.6)$$

Here,  $R_L$  is the total sensor resistance consisting of the inductor resistance, capacitor resistance and circuit resistance, which is briefly discussed by Musunuri et al. in [36].

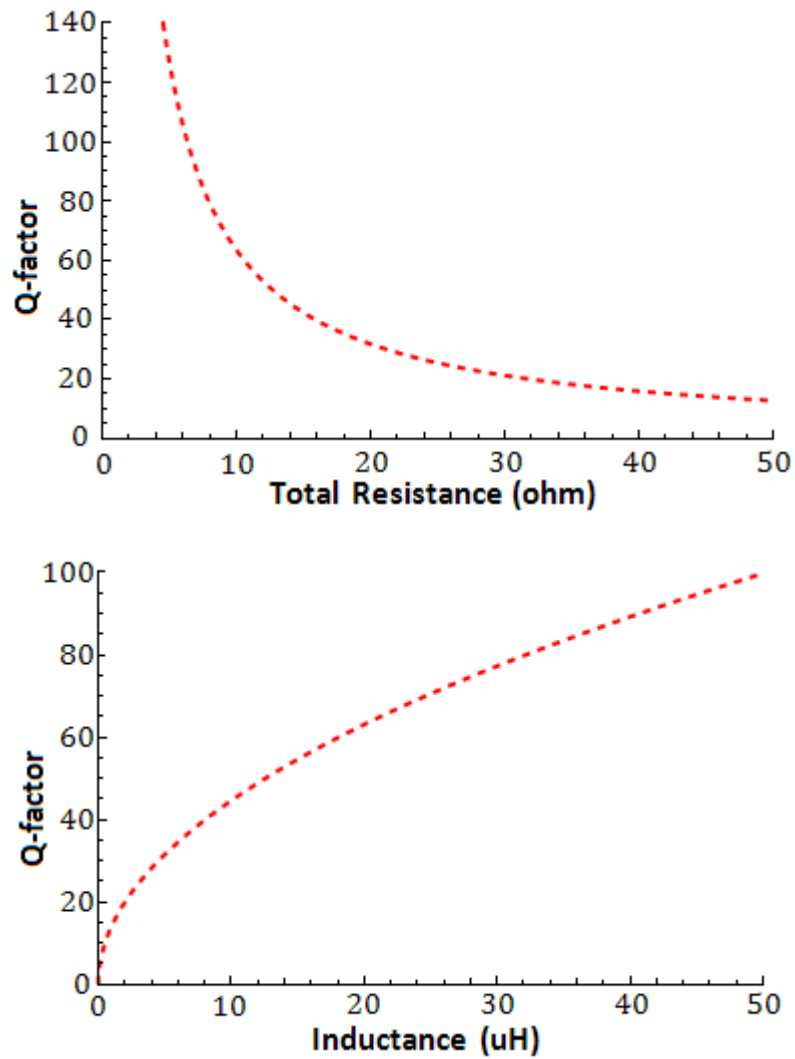


**Figure 4-5  $Q$ -factor vs. Resistance & Inductance**

Figure 4-5 depicts the variation of the  $Q$ -factor with respect to total sensor resistance and sensor inductance. This simulation shows that minimizing the total resistance and maximizing sensor inductance will improve the  $Q$ -factor. In real case, increase the turns of the sensor inductor will increase the  $L_S$  and  $R_L$ . The  $Q$ -factor  $Q$  will get the maximum value when turns of the sensor inductor  $n = 8$ .

#### **4.4 Conclusions**

In this chapter, design principle of spiral inductor of the sensor and electrical model of the resonant circuit is presented. The key characteristic sensor performance factor such as  $Q$  factor and coupling factor with respect to design parameter has been analyzed. In order to achieve high performance wireless system, characterized with a high  $Q$ -factor and a maximized communication distance, one should seek maximizing sensor inductance and radius of sensor inductor while minimizing the sensor resistance, the radius of the reader antenna or reader inductance. The spiral inductor with eight turns was made of copper wire leads and connected to the electrodes of the capacitor. The diameter of the round copper wire was  $0.674\text{ mm}$  and the radius of the inductor was  $2.7\text{ cm}$ . The area of the electrode plate was  $23\text{ mm}^2$ .

## 5 REMOTE POWER AND WIRELESS COMMUNICATION

Moreover, the principle of the inductive power communication is present. The energy transfer, which is based on the interaction between the spiral inductor on the sensor and the coil antenna on the reader, will be demonstrated. Moreover, the electrical model of resonant circuit is used to simulate resonant frequency variations in response to crack information.

### 5.1 Inductive Powering

Uses of spiral inductors and capacitors to form resonant circuits have been used for various measurement applications. This wireless interrogation and remote powering is achieved through an inductively powered system which is generating a time varying electromagnetic field [34] based on Faraday's induction.

The simplified model of the spiral inductor and interdigital capacitor with a nearby reader coil for inductive powering is demonstrated in Figure 5-1 as a LC resonator with self resistance. In this Figure,  $R_R$  is the resistance existing in the reader side and  $R_S$  is the resistance in the sensor circuit. A time variant current  $I_1$  enables the resonant frequency to vary in time with a given interval,  $T$ ;  $C_R$  is the capacitance of the reader circuit that is used to maximize the current applied through the reader antenna; and  $M$  is the mutual inductance. The frequency of this current  $\omega$  is a linear function with respect to time and can be given by:

$$\omega = \Delta\omega \cdot t + \omega_0 (T \leq t \leq T + \Delta t) \quad (5.1)$$

Once this current with a varying frequency applied to the primary coil, a varying magnetic field generated around this coil. Based on Faraday's law, induced voltage is generated on the remotely placed sensor.

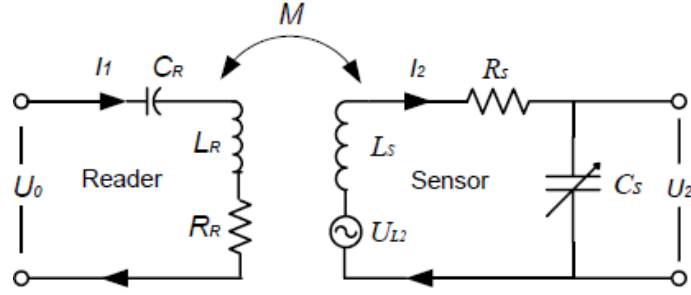


**Figure 5-1 Inductively Coupled Circuit**

If  $U_{L2}$  indicates the voltage induced in the sensor inductor, it can be calculated by equation 5.2:

$$U_{L2} = j\omega M I_1 \quad (5.2)$$

The voltage  $U_2$  on the capacitor of the sensor can be expressed as follows:

$$U_2 = U_{L2} - j\omega L_S I_2 - R_S I_2 \quad (5.3)$$

And the current is determined by equation 5.4:

$$I_2 = j\omega C_S U_2 \quad (5.4)$$

Therefore, by solving Equation 5.3 and 5.4, the voltage across the planar capacitor  $U_2$  becomes

$$U_2 = \frac{U_{L2}}{1 + (j\omega L_S + R_S)j\omega C_S} \quad (5.5)$$

The voltage  $U_{L2}$  will be induced when the planar resonance sensor placed in the time-variant magnetic field of the reader antenna  $L_R$ . Once the capacitance of the sensor changed due to crack extension,  $U_2$  will change accordingly and then a change is detected in the voltage  $U_0$  across the reader.

Therefore, at a certain frequency, the capacitance change can be monitored as long as the variation of voltage it induced is measurable. However, in most cases, the change in voltage is extremely small and is beyond the range of general detection device. Since the capacitance variation will modify the planar resonator's resonant frequency  $f_r$ , generally, instead of measuring the voltage variation at a certain frequency, we use a signal to generate a periodical sweep in frequency around the sensor's natural frequency to measure the frequency variation. This reflected sensor

impedance changes in response to sensor capacitance changes when the reader's frequency is swept. When the excitation frequency matches the sensor side resonant frequency, a sudden increase in the sensor impedance  $Z'_S$  occurs. In this way, a very small variation in the impedance can be measured.

The voltage response of the reader's antenna coil verses sweep frequency without the presents of a sensor can be calculated by

$$U_0 = (j\omega L_R + R_R)I_1 \quad (5.6)$$

And the voltage response of the reader's antenna coil verses sweep frequency with the presents of a sensor can be calculated by

$$U_0 = \left( j\omega L_R + R_R + \frac{\omega^2 k^2 L_R L_S}{j\omega L_S + R_S + \frac{1}{j\omega C_S}} \right) I_1 \quad (5.7)$$

The coefficient  $k$  given in equation 4.3 is defined by:

$$k = \left( \frac{r_S r_R}{d^2 + r_R^2} \right)^{\frac{3}{2}} \quad (4.3)$$

When the voltage appears as an abrupt change, it indicates the point where the resonant frequency lies in. Generally speaking, the resonant frequency occurs at the peak of the voltage plot during a sweep frequency range. The expression of the resonant frequency is defined by the following equation:

$$f_r = \frac{1}{2\pi\sqrt{L_S C_S}} \quad (5.8)$$

Here  $L_S$  and  $C_S$  were defined according to equation 3.6 and 4.2, respectively.

## 5.2 Modeling and Simulation

The power delivery and wireless data communication scheme has been illustrated in Figure 1-2. As shown in the figure, in a proposed common practice, an oscillating magnetic wave will be sent out through the remote reader, and will be received by sensor inductor by inductive link, thus power on the LC sensor. In the meantime, the frequency modification of LC sensor induced by crack formation and propagation can

be detected by the remote reader.

The remote reader across inductive powering will generate a magnetic field induced by an alternating current and the proposed crack sensors will be placed within that magnetic field as shown in Figure 5-2. In this resonant circuit,  $Z_R$  and  $Z_S$  are the reader and sensor inherent impedances respectively.  $R_R$  and  $R_S$  are the self resistances of the reader and the sensor circuit.  $C_R$  is the reader capacitance, which is used to maximize the current applied through the reader antenna;  $C_S$  is the sensor capacitance, which is sensitive to the crack formation and propagation.  $Z_S'$  is the reflected impedance of the sensor, and,  $M$  is the mutual inductance [35].

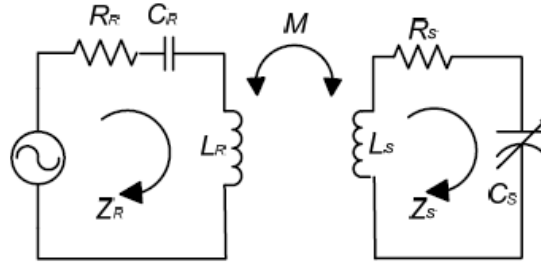


**Figure 5-2 Inductive Coupled Reader and LC Sensor**

The equivalent circuit diagram of the resonant circuit of the reader with the inductive coupled sensor is shown in Figure 5-3.

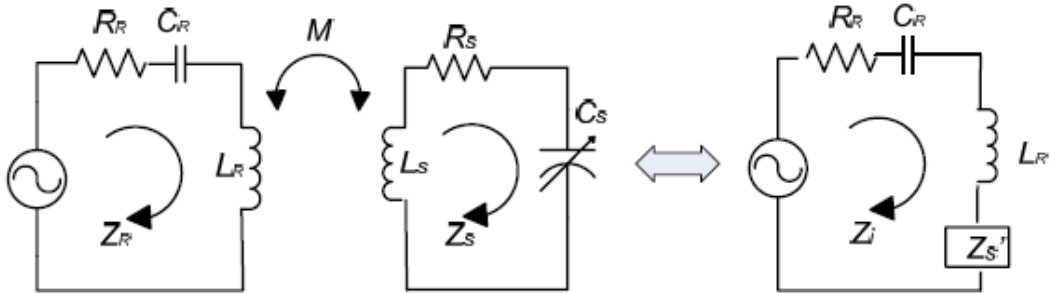


**Figure 5-3 Equivalent Circuit Diagram of Wireless Telemetry System**

The impedance of the resonant circuit of the reader is given by:

$$Z_R = j\omega L_R + R_R + \frac{1}{j\omega C_R} \quad (5.9)$$

In addition, the impedance of the sensor side can be expressed as:

$$Z'_S = \frac{(\omega M)^2}{j\omega L_S + R_S + \frac{1}{j\omega C_S}} = -\frac{\omega^2 k^2 L_R L_S}{j\omega L_S + R_S + \frac{1}{j\omega C_S}} \quad (5.10)$$

Where  $k$  is the coupling factor, defined by equation 4.3

$$k = \left( \frac{r_S r_R}{d^2 + r_R^2} \right)^{\frac{3}{2}} \quad (5.11)$$

The sensor interaction can be seen as a load variation  $\Delta Z'_S$  placed in series with the inductance antenna, defined by:

$$\Delta Z'_S = \frac{\omega^2 k^2 L_R L_S}{j\omega L_S + R_S + \frac{1}{j\omega(C_S + \Delta C_S)}} \quad (5.12)$$

The input impedance seen from the reader side is defined by:

$$Z_i = Z_R + Z'_S \quad (5.13)$$

Using the equation 5.9 and 5.10 into 5.13, we have the input impedance seen from the reader defined by:

$$Z_i = j\omega L_R + R_R + \frac{1}{j\omega C_R} + \frac{\omega^2 k^2 L_R L_S}{j\omega L_S + R_S + \frac{1}{j\omega(C_S + \Delta C_S)}} \quad (5.14)$$

Therefore, the input impedance seen from the reader can be calculated by 5.14.

The reflected impedance  $Z'_S$  multiplied by the current is equivalent to the voltage drop caused by the sensor side circuit.

Actually, instead of measuring the voltage change at a certain frequency, we can use a signal to generate a periodical sweep of the frequency around the sensor's natural frequency to measure a frequency variation. This reflected sensor impedance changes in response to sensor capacitance changes when the reader's frequency is swept. When the excitation frequency matches the sensor side resonant frequency, a sudden increase in the sensor impedance  $Z'_S$  occurs. Figure 5-4 shows the magnitude of impedance and phase of this reflected sensor impedance  $Z'_S$  in response to the sweeping frequency changes, the simulation is calculated by the parameter values listed in Table 5.1.

**Table 5-1 Electrical Parameter Values for Interdigital Crack Sensor**

PARAMETER	SYMBOL	PDMS
Sensor Nominal Capacitance	$C_s$	20.1pF
Sensor Inductance	$L_s$	8.2uH
Resonant Frequency	$f_0$	12.4MHz
Sensor Resistance	$R_s$	0.4Ω
Reader Inductance	$L_R$	0.117uH
Reader Radius	$r_R$	2.7cm
Inductor Radius	$r_s$	2.7cm
Coupling Distance	D	1cm
Nominal Coupling Factor k	K	s

The Figure 5-5 shows the magnitude of impedance of the sensor impedance  $Z_s$  in response to the sweeping changes, the simulation is calculated by the parameter values in table I. It is shown in Figure 5-5, when crack start propagating, the peak of the input impedance  $Z_s$  will move toward the right of the plot, which suggest the resonant frequency increases.

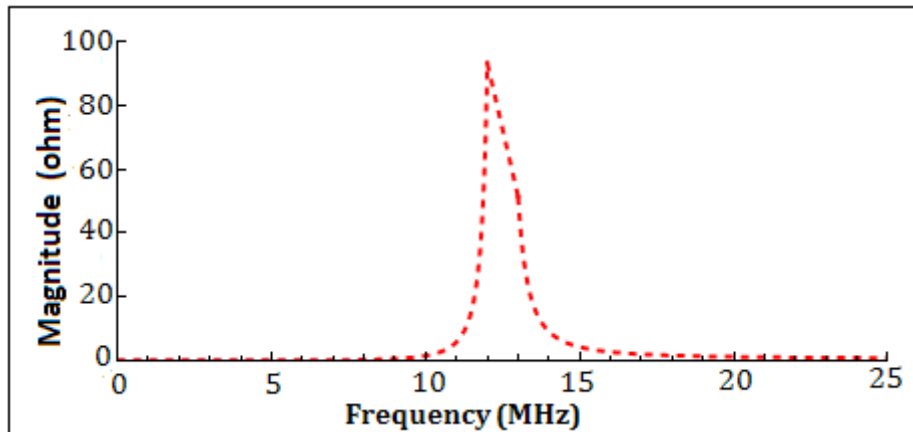


**Figure 5-4 Magnitude & Resonant Frequency**

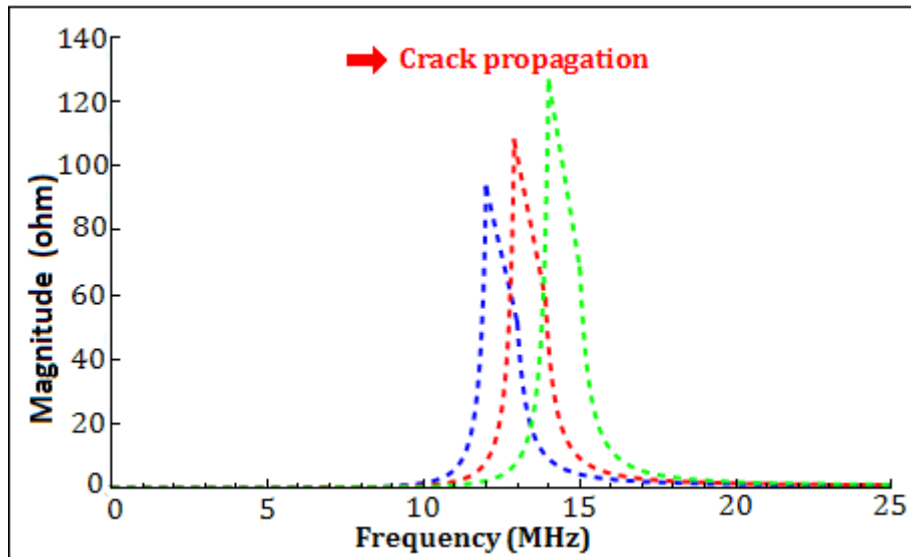


Figure 5-5 Resonant Frequency of Input Impedance vs. Crack propagation

### 5.3 Resonant Frequency

In general, a resonant circuit is comprised of elements that dissipate energy and store energy: resistive components dissipate energy and reactive components store energy. Stored energy gives rise to a phase shift between the voltages and currents in a system. It is customary to employ complex variables to describe such systems, such that a measured real quantity is in phase with the excitation signal and a measured imaginary value is 90 degrees out of phase with the excitation signal. A positive value of reactance is defined as inductive and a negative value of reactance is defined as capacitive. Any passive circuit has the following properties at resonance:

(1) At resonance, inductive stored energy is equal to the capacitance stored energy. Since they are of opposite signs, the reactance cancels each other.

(2) Since the reactance vanishes at resonance, the observed impedance of the circuit is purely resistive. Mathematically, this implies that the measured impedance is thus purely real with zero phase shifts.

(3) Provided that the losses in the circuit are small relative to the reactance, the magnitude of the measured voltages and currents shall exhibit a pronounced peak (or dip) in the vicinity of resonance.

The expression of the resonant frequency is given by the following equation:

$$f_r = \frac{1}{2\pi\sqrt{L_S C_S}} \quad (5.8)$$

This resonant frequency is defined in terms of sensor electrical parameters and indicates the peak of magnitude and zero crossing point of the phase of the reflected sensor impedance,  $Z_s'$ , as shown in Figure 5-4.

In order to readily detect the resonant frequency from the reader's side, the reflected impedance,  $Z_s'$ , should be high enough. If the changes of reflected impedance from the sensor  $Z_s'$ , are smaller than those of inductance from the antenna, most of the voltage drop will occur across the antenna. This will bury the change of reflected impedance,  $Z_s'$ , caused by the remote sensor. For this reason, the  $Q$ -factor and coupling coefficient should be high enough to make sure that the resonant frequency can be detected.

## 5.4 Conclusions

In this chapter, the energy transfer mechanism is demonstrated, which is based on the interaction between the inductor of the sensor and the coil antenna of the reader. Electrical model of resonant circuit is used to simulate resonant frequency variations in response to crack information. In order to locate the resonant frequency in the detectable range, a model with respect to the geometric dimensions of the planar capacitor and spiral inductor is built.

## **6 SENSOR CHARACTERIZATION AND EXPERIMENT RESULTS**

A proof test was performed to show that the IDC sensing system can measure and record the resonance frequency change due to the propagation of a crack. In this chapter, sensor prototypes fabrication is discussed. A brief description of the crack testing system setup will be presented. The crack measurement and sensor calibration will be discussed.

### **6.1 Fabrication interdigital crack sensor**

In this section we will discuss sensor fabrication using micro-electromechanical system (MEMS) fabrication technique. For the fabrication of the interdigital crack sensor, we will use the photolithography process which is one of the most important approaches in bulk micromachining. Photolithography is a process used in micro-fabrication to selectively remove parts of a thin film. It uses light to transfer a geometric pattern from a photomask to a light-sensitive chemical (photoresist) on the substrate. A series of chemical treatments then engraves the exposure pattern into the material underneath the photoresist.

For the fabrication of IDC crack sensor we will use the following materials: The pattern-transfer target material for the main circuit of the sensor in DuPont Pyralux, AC single copper-card laminate which is all-polyimide composite of polyimide film on copper foil. Polyimide base substrate thickness are available from  $25\mu\text{m}$  to  $45\mu\text{m}$ , Rolled-annealed (RA) copper foil thickness from  $18\mu\text{m}$  to  $35\mu\text{m}$ , and electro-deposited (ED) copper foil thickness from  $25\mu\text{m}$  to  $45\mu\text{m}$ . The basic procedure for Photolithography is briefly outlined in below:

1. Cleaning. The laminated copper clad is cleaned with a solvent to remove the contaminants on the surface. Clean surface condition would offer a better contact for the applied photo resist (PR) and provide a good circuit condition.

2. Preparation. Apply a thin layer of PR on the surface of the copper clad and make it spread all over the surface instead of just dropped on one point on the surface. In order to get a uniform thin layer, a spin coating which typically runs at 1200 to 4800 RPM for 30 to 60 seconds is used.

3. Exposure. A transparent photographic film which contains the pattern of the desired circuit is aligned on the soft baked copper clad. Make sure that the ink side on the pattern film is the side that attached to the PR. Turn on the UV light and start the time for 90 seconds.

4. Developing. Remove the mask pattern film and replace the copper clad into the developer solvent which is 1:1 solution of AZ developer and deionizer water. Hold the clad with tweezers and agitate mildly until the PR which is expose to the UV light has been fully dissolved. A legible patterned part which is the same as the mask pattern is left on the copper.

5. Etching. Leave the copper clad into the hard baking oven at 120°C for 60 minutes. Cool it and immerse it into the solutions of a board etchant. Hold the clad with tweezers and agitate mildly until the copper, which is not covered by the hard-baked PR, is completely etched away.

Major procedures are briefly shown below in Figure 3-25.

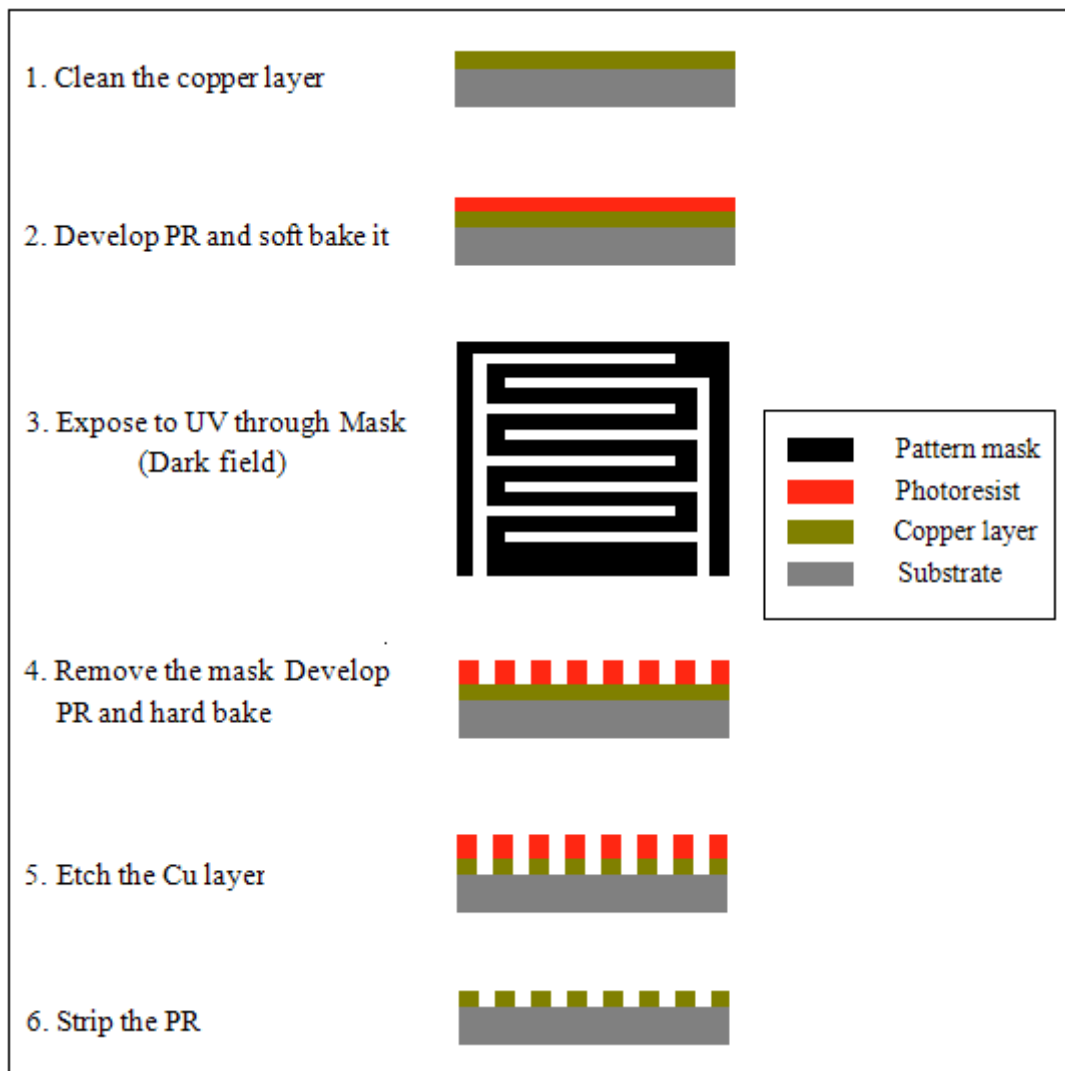


**Figure 6-1 Splitting of the proposed IDC sensor**

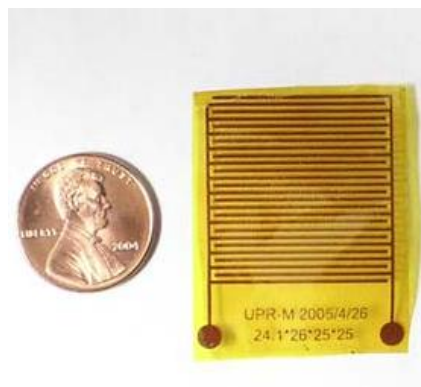


**Figure 6-2 Fabricated sensing element prototype**

## 6.2 Testing System Setup

### 6.2.1 Pretest procedure

Before the test, a fabricated crack sensor is bonded to a small steel test coupon, which is shown in Figure 6-3. A crack propagation pattern was chosen due to its capacitance change in response to crack propagation. The gap between its two neighboring parallel fingers is  $800\mu\text{m}$ , which sets the lowest measuring limit of the crack propagation increment. In other words, no crack propagation increments less than  $800\mu\text{m}$  can be detected by this crack sensor.

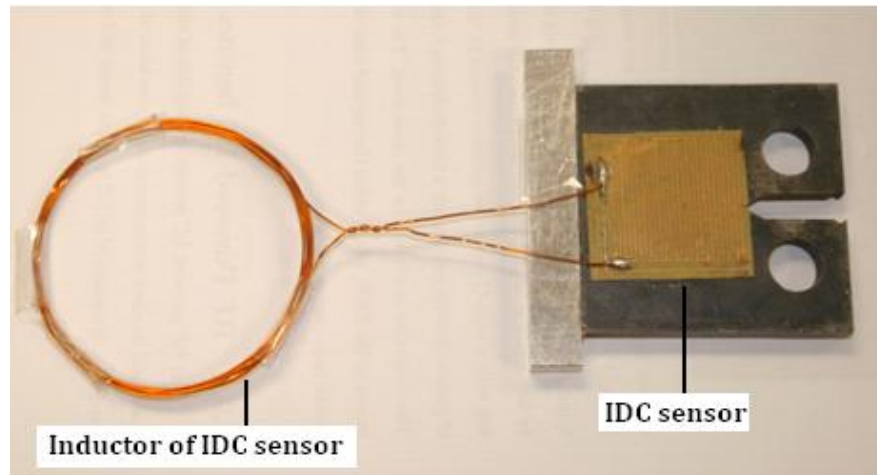


**Figure 6-3 Crack sensor bonded to the testing coupon**

In standard experiment configuration, a crack would grow and propagate through the portion of the coupon to which the sensor was attached. The testing apparatus applied force to the coupon by applying and releasing tension through two circular attachment points at the top and bottom of the test coupon. All displacements and forces are measured with respect to these two points. However, due to the fact that abovementioned apparatus is not available in this study, an alternative procedure was put into place.

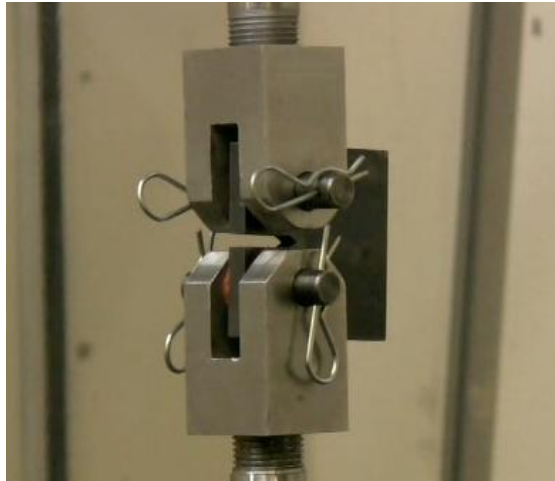


**Figure 6-4 Propose test coupon mounted in test apparatus**

### *6.2.2 Actual crack test setup*

Proposed passive wireless sensor for calibration is attached to the specimen by special adhesive for crack measurement. Fabricated crack sensor with a test coupon is fastening with a clamped end.

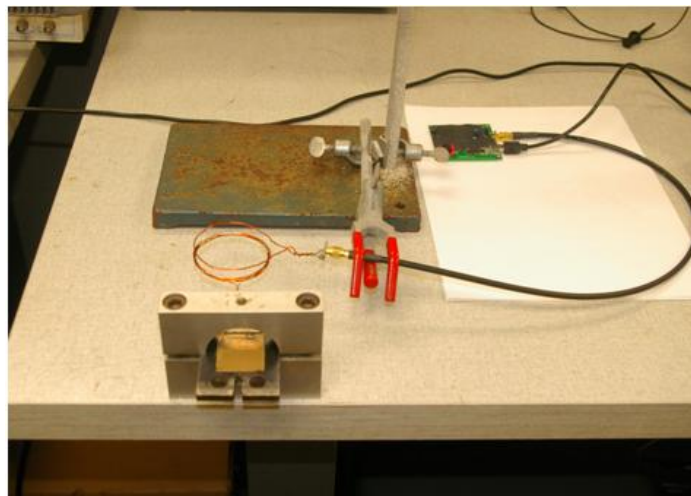


**Figure 6-5 Sensor coil vs. reader antenna**

The antenna coil of reader is put right above the sensor coil, which is shown in Figure 6-5. A careful adjustment of the distance between sensor reader and antenna coil was conducted to reach an optimal distance which ensures the efficient the wireless data communication and remote power transfer.

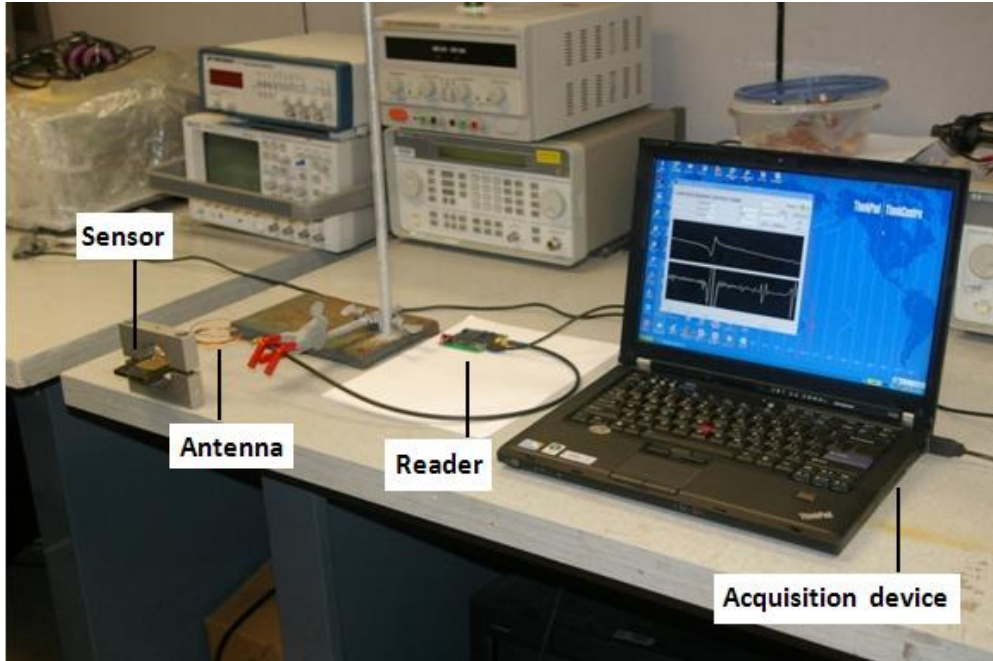


**Figure 6-6 Experiment setup**

The complete test system is shown in Figure 6-6. The test signal can be recorded by reader. Then the data is transmitted to computer and can be read out by software Serial Port Monitor which is a professional and powerful system utility for COM ports monitoring. Real time monitoring was carried out by software named TagSense. The frequency response can be plot out on screen while the sensor capacitance varies with respect to the crack formation and propagation. The major test parameter is listed in table 6-1. Related experimental results and system characterization are present in the next section.

**Table 6-1 Frequency data set for the experiment**

Data setup for frequency sweeping	Value
Start Frequency	5.4MHz
Stop Frequency	30MHz
Step Frequency	0.2MHz

## 6.3 Sensor Performances Characterization

In order realize the crack propagation path discussed in Chapter 3, which involves different crack position and corresponding propagation angles, a cutting saw is utilized to generate crack and control crack propagation path in this experiment.

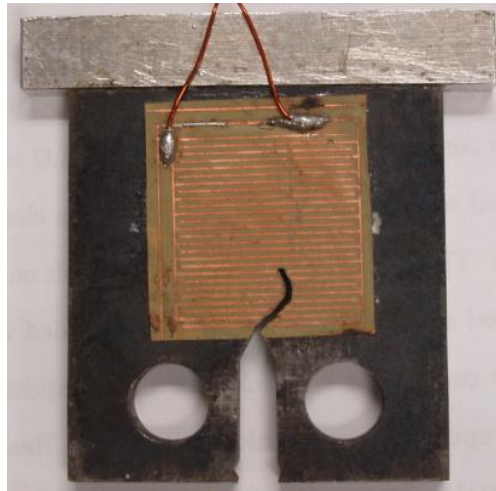


**Figure 6-7 Actual crack path (N=8)**

A photograph of an actual crack propagation path generated by the cutting saw is shown in Figure 6-7.

### 6.3.1 Theoretical calculation

In order to simulate the real process of the experiment, we make following assumptions:

1. When the deformation of IDC sensor happens, we assume the size of the gap width and the finger length will stay the same;
2. For the convenience of theoretical treatment, we consider the angle of crack propagation between two fingers doesn't change during the experiment.
3. The thickness as well as the length of the electrodes is considered to be constant when the deformation occurs.
4. The capacitance at the electrode end gap is not small enough to be ignored compared to the major capacitance between the electrodes.

Based on the crack position value obtained from the actual crack site, a simulation was conducted. The major results are presented in Figure 6-8.

The sensitivity of the IDC crack sensor can be defined as the slope of the curve in Figure 6-8

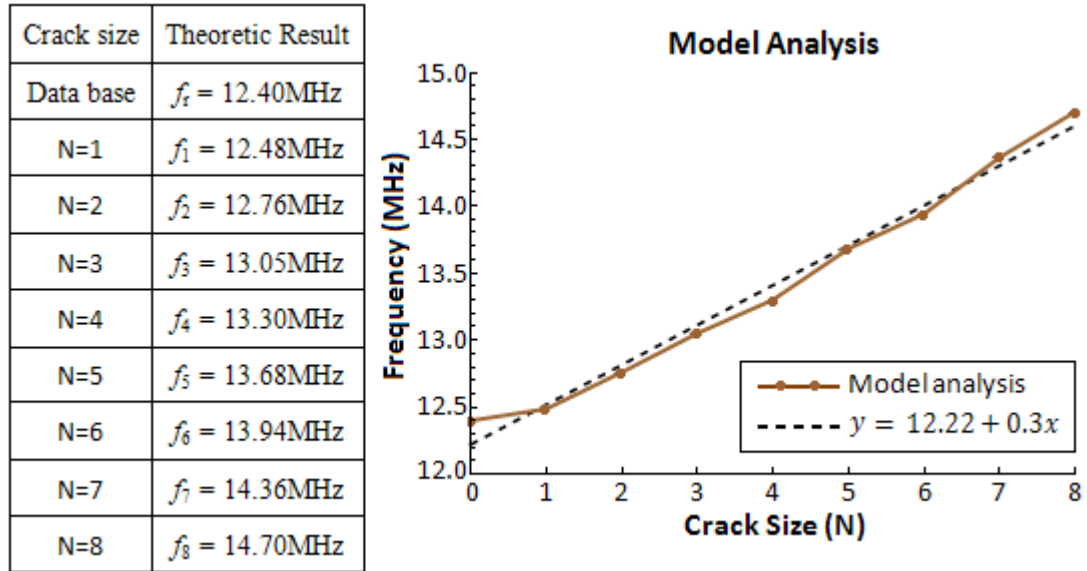


**Figure 6-8 Resonant frequency of theoretic result**

As can be seen from the Figure 6-8, the resonant frequency of sensor increases linearly as the crack size increase.

### 6.3.2 Experiment result

The impedance of the sensor loop versus the sweeping frequency test signal with different crack size is plotted out in Figure 6-9. Inspection of the figure suggested that with the increase of crack size, the resonant frequency of sensor increases as well. The actual value of frequency variation with respect to crack size is shown in Figure 6-10.

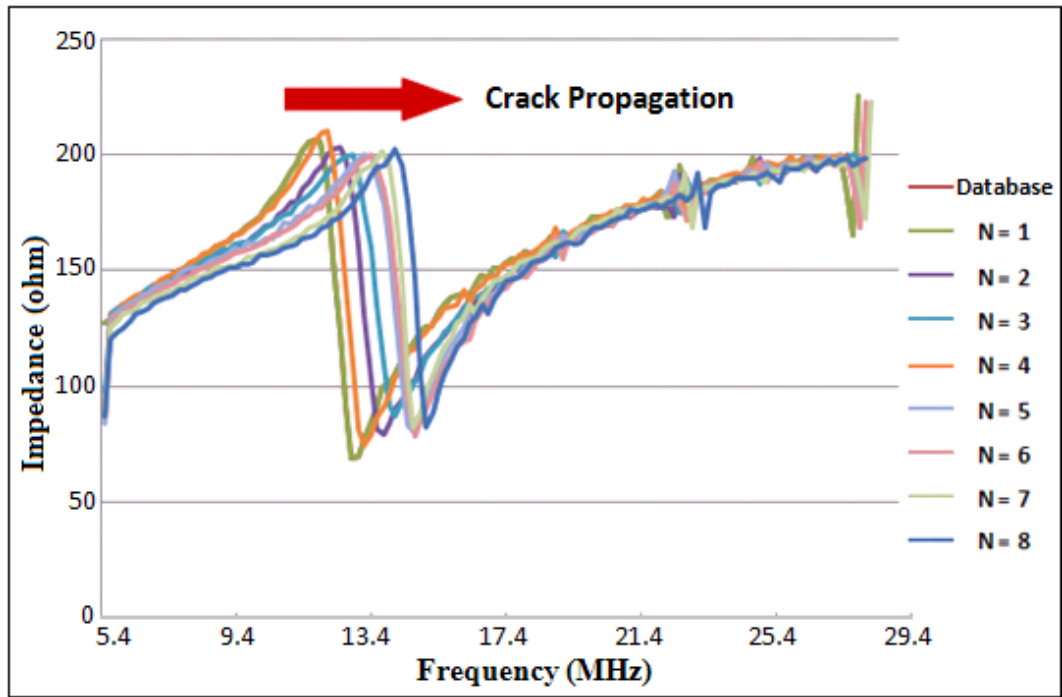


Figure 6-9 Resonant frequency of IDC sensor with crack propagation

Crack size	Experiment Result
Data base	Peak: $f_t = 12.40\text{MHz}$
N=1	Peak: $f_1 = 12.40\text{MHz}$
N=2	Peak: $f_2 = 12.80\text{MHz}$
N=3	Peak: $f_3 = 13.00\text{MHz}$
N=4	Peak: $f_4 = 13.40\text{MHz}$
N=5	Peak: $f_5 = 13.80\text{MHz}$
N=6	Peak: $f_6 = 14.00\text{MHz}$
N=7	Peak: $f_7 = 14.40\text{MHz}$
N=8	Peak: $f_8 = 14.80\text{MHz}$

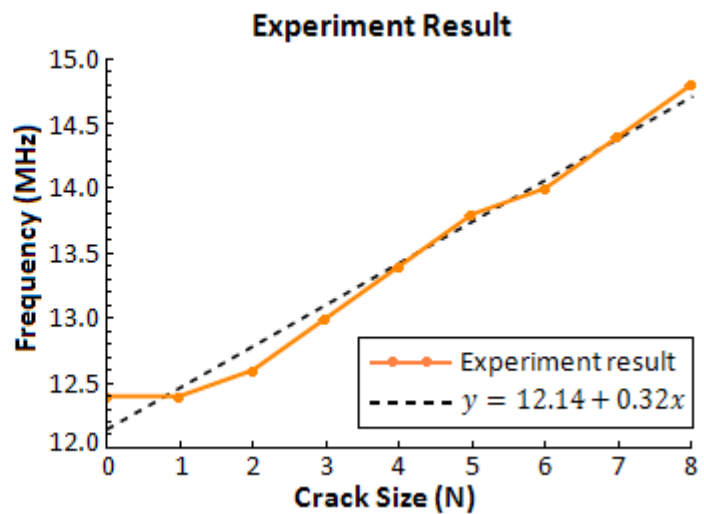
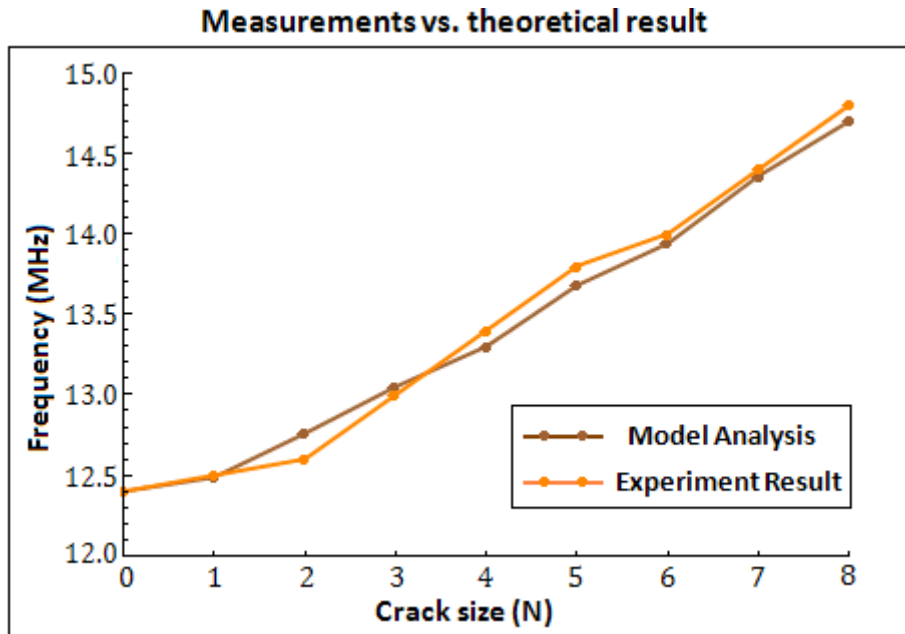


Figure 6-10 Resonant frequency of experimental result

### 6.3.3 Measurements vs. theoretical result

The comparison between theoretical simulation result and experiment result is shown in the Figure 6-11. One can see that the experiment result and simulation results agree to each other very well.



**Figure 6-11 Comparison between experiment result and theoretic result**

The reason for discrepancy between the theoretical results and the experimental results might be attributed to the fact that the width of the crack too big compared to the real situation. Another possible reason to cause the discrepancy is that the set sweeping frequency step is 0.2MHz, which render the device is insensitive to some small frequency change induced by crack propagation between two neighboring finger electrodes. Other factor is the noise cause by the reader's antenna, this noise made the resonant frequency changed a bit.

## **6.4 Conclusions**

An experiment was conducted to demonstrate the feasibility of LC crack sensor made of IDC for the application of wireless crack monitoring. The crack induced frequency response can be efficiently detected. The experimental result is in good agreement to the corresponding theoretical prediction, which indicates the design of sensor is sound fundamentally.

## **7 CONCLUSIONS AND FUTURE WORK**

### **7.1 Conclusions**

This research project has developed a novel passive wireless crack sensor, which has the structure with two major parts: a capacitor which is a crack sensing element and an inductor which works as a passive power source and data communication element. These two components work together as an LC resonator to realize the wireless crack sensing and remote power, eliminating the need for wire connection. The sensor prototype was then successfully fabricated to prove the concept of a crack sensing device using passive wireless communication.

Research contributions achieved by this project can be summarized as follows:

An innovative passive wireless sensor scheme has been successfully demonstrated;

Sensor performance was analyzed;

The sensor prototype was developed and calibrated.

The effective design of planar resonators for wireless sensing applications requires a process to obtain a geometry that optimizes application requirements. Modeling and simulation were performed in order to minimize sensor size, maximize the detection distance, quality factor, and sensor sensitivity.

### **7.2 Future work**

There are couples of researches can be extended as future works, which can be concluded as the followings:

Investigate the IDC crack sensor with better sensitivity, linearity and minimized sensor size.

Extend the communication distance of the crack sensor;

Design and fabricate the dissymmetry structure crack sensor able to sensing the centre crack initial position and more sensitivity to sensing the crack extension in different angle.

## REFERENCE

- [1] P.C. Chang, A. Flatau, and SC Liu. Review paper: health monitoring of civil infrastructure. *Structural Health Monitoring*, 2(3):257, 2003.
- [2] F.K. Chang. *Structural health monitoring: current status and perspectives*. CRC, 1997.
- [3] H. Sohn, C.R. Farrar, FM Hemez, DD Shunk, DW Stinemates, BR Nadler, et al. A review of structural health monitoring literature: 1996{2001. Los Alamos National Laboratory, Los Alamos, NM, 2004.
- [4] C. Sekine-Pettite. *Structural Health Monitoring*.
- [5] Gongkang, F. (2004). Non Destructive Testing For Steel Highway Bridges, NDT Methods Applied to Fatigue Reliability Assessment of Structures, J. Mohammadi, ed., American Society of Civil Engineers, Reston, VA, 23-31.
- [6] Moore, P. O. (1998). *Nondestructive Testing Handbook*, C. N. Jackson Jr, Sherlock, C. N., ed., American Society for Nondestructive Testing.
- [7] Son, J., Mohammadi, J. (2004). NDT Methods Applied to Fatigue Reliability Assessment of Structures, A Review of Non-destructive Test Methods for Bridges, J. Mohammadi, ed., American Society of Civil Engineers, Reston, VA, 122-138.
- [8] Rakow, A., Chang, F. K. (2007). "An In-Situ Sensor Design for Monitoring Fatigue Damage in Bolted Joints." 6th International Workshop on Structural Health Monitoring (IWSHM), DEStech Publications, Inc, Stanford, CA.
- [9] Lee, D. C., Lee, J. J., Kwon, I. B., Seo, D. C. (2001). "Monitoring of Fatigue Damage of Composite Structures by Using Embedded Intensity-based Optical Fiber Sensors." *Smart Materials and Structures*, 10(2), 285-292.
- [10] Zhang, Y. (2006a). "In Situ Fatigue Crack Detection using Piezoelectric Paint Sensor." *Journal of Intelligent Material Systems and Structures*, 17(10), 843-852.
- [11] Lee, Y. L., Pan, J., Hathaway, R. B., Barkey, M. E. (2005). *Fatigue Testing and Analysis: Theory and Practice*, Elsevier Inc.

- [12] Broek, D. (1986). *Elementary Engineering Fracture Mechanics*, Kluwer Academic Publishers, Dordrecht, Netherlands.
- [13] M. Enmark, G. Lucas, Gr. Odette, An electric-potential drop technique for characterizing part-through surface cracks, *J. Nucl. Mater.* 191 (Part B) (1992) 1038–1041.
- [14] S.Z. Zhang, Y.J. Yan, Z.Y. Wu, Electric potential detection for structural surface crack using coating sensors, *Sensors and Actuators A* 137 (2007) 223–229
- [15] Casas, J. R., Cruz, P. J. S. (2003). "Fiber Optic Sensors for Bridge Monitoring." *ASCE Journal of Bridge Engineering*, 8(6), 362-373.
- [16] I. Leung, C.K.Y., *Fiber optic sensors for concrete structures: the future*, *Non-destructive Testing and Evaluation*, Vol.34, pp 85-94, 2001
- [17] D.N. Alleyne, P. Cawley, The interaction of Lamb waves with defects, *IEEE Trans. Ultrason. Ferroelectr. Freq. Control* 39 (1992) 381–397.
- [18] T. Kundu, Guided waves for plate inspection, in: T. Kundu (Ed.), *Ultrasonic Nondestructive Evaluation*, CRC Press, Boca Raton, FL, 2004, chap. 4.
- [17] Hiroshi Tsuda , Jung-Ryul Lee, Yisheng Guan, Junji Takatsubo, Investigation of fatigue crack in stainless steel using a mobile fiber Bragg grating ultrasonic sensor, National Institute of Advanced Industrial Science and Technology, Japan
- [19] H. Tsuda, Ultrasound and damage detection in CFRP using fiber Bragg grating sensors, *Comp. Sci. Tech.* 66 (2006) 676–683.
- [20] Fisher, J. W., Kulak, G. L., Smith, I. F. C. (1998). *Fatigue Primer for Structural Engineers*, National Steel Bridge Alliance, USA.
- [21] Chase, S. B., Washer, G. (1998). "Nondestructive Evaluation for Bridge Management in the Next Century." *Public Roads*, 61(1), 16-25
- [22] Mathew Kotowsky, Charles Dowding, Ken, Fuller, *Wireless sensor networks to monitor crack growth on bridges*, Infrastructure Technology Institute
- [23] Chan, T. H. T., Li, Z. X., Ko, J. M. (2001). "Fatigue Analysis and Life Prediction of Bridges with Structural Health Monitoring Data - Part II: Application." *International Journal of Fatigue*, 23, 55-64.

- [24] Li, Z. X., Chan, T.H.T., Ko, J.M. (2001). "Fatigue Analysis and Life Prediction of Bridges with Structural Health Monitoring Data - part I: Methodology and Strategy." *International Journal of Fatigue*, 23, 45-53.
- [25] Mohammadi, J., Guralnick, S. A., Polepeddi, R. (2004). Use of Stress Range Data in Fatigue Reliability Assessment of Highway Bridges, *NDT Methods Applied to Fatigue Reliability Assessment of Structures*, J. Mohammadi, ed., American Society of Civil Engineers, Reston, VA, 56-71.
- [26] Md.Kamrul Hassan, Muhammad Fauzi Mohd Zain, Micro Crack Monitoring in Common Bridge Structure by Smart Wireless Sensor, *Proceedings of the Regional Engineering Postgraduate Conference 2009 20-21 October 2009*
- [27] Vishay. (2008) "Special Use Sensors - Crack Propagation Sensors", <[www.vishaymg.com](http://www.vishaymg.com)> (June 16, 2008).
- [28] Zhang, Y. H., Tubby, P. J. (2006b). "Development of a Fatigue Sensor for Welded Steel Structures." *International Conference on Residual Fatigue Lifetime Extension of In-Service Structures*, JIP, Paris, France.
- [29] Chase, S. B. (2005). The Role of Sensing and Measurement in Achieving FHWA's Strategic Vision for Highway Infrastructure, *Sensing Issues in Civil Structural Health Monitoring* F. Ansari, ed., Springer, Netherlands, 23-32.
- [30] Peng Xu, Songling Huang, Wei Zhao, Differential Eddy Current Testing Sensor Composed of Double Gradient Winding Coils for Crack Detection, Department of Electrical Engineering Tsinghua University Beijing, China
- [31] Technology Enable Active Learning MIT, Mit Physics 8.02t electricity magnetism Course notes, May 2006.
- [32] Rui Igreja and C. J. Dias, "Analytical Evaluation of the Interdigital Electrodes Capacitance for a Multi-Layered Structure", *Sensors and Actuators A*, vol.112, pp.291-301, January 2004
- [33] Frederick W. Grover, "Inductance Calculations: Working Formulas and Tables", Dover Publications, Inc., New York, 1946.

- [34] Sunderarajan S. Mohan, Maria del Mar Hershenson, Stephen P.Boyd, and Thomas H.Lee, “Simple Accurate Expressions for Planar Spiral Inductances”, IEEE, Journal of Solid-State circuits, vol.34, pp.1419-1424.
- [35] Ya Wang, A passive wireless temperature sensor for harsh environment application, 2007
- [36] Surya Musunuri, Patrick L. Chapman, Jun Zou, and Chang Liu, “Design Issues for Monolithic DCDC Converters”, IEEE Transactions on Power Electronics, vol.20, no.3, May 2005, pp.639-649.
- [37] K. Finkenzeller, RFID Handbook, Fundamentals and Applications in Contactless Smart Cards and Identification, 2nd ed, John Wiley & Sons Ltd, 2003.